

BACKGROUND MODELING FOR DOUBLE HIGGS BOSON PRODUCTION: DENSITY RATIOS AND OPTIMAL TRANSPORT

BY TUDOR MANOLE^a, PATRICK BRYANT^d, JOHN ALISON^e, MIKAEL
KUUSELA^b, AND LARRY WASSERMAN^c

*Department of Statistics and Data Science and NSF AI Planning Institute for Data-Driven Discovery in Physics,
Carnegie Mellon University*

^atmanole@andrew.cmu.edu; ^bmkuusela@andrew.cmu.edu; ^clarry@stat.cmu.edu

*Department of Physics and NSF AI Planning Institute for Data-Driven Discovery in Physics,
Carnegie Mellon University*

^dpbryant2@andrew.cmu.edu; ^ejohnalison@cmu.edu

We study the problem of data-driven background estimation, arising in the search of physics signals predicted by the Standard Model at the Large Hadron Collider. Our work is motivated by the search for the production of pairs of Higgs bosons decaying into four bottom quarks. A number of other physical processes, known as background, also share the same final state. The data arising in this problem is therefore a mixture of unlabeled background and signal events, and the primary aim of the analysis is to determine whether the proportion of unlabeled signal events is nonzero. A challenging but necessary first step is to estimate the distribution of background events. Past work in this area has determined regions of the space of collider events where signal is unlikely to appear, and where the background distribution is therefore identifiable. The background distribution can be estimated in these regions, and extrapolated into the region of primary interest using transfer learning of a multivariate classifier. We build upon this existing approach in two ways. On the one hand, we revisit this method by developing a powerful new classifier architecture tailored to collider data. On the other hand, we develop a new method for background estimation, based on the optimal transport problem, which relies on distinct modeling assumptions. These two methods can serve as powerful cross-checks for each other in particle physics analyses, due to the complementarity of their underlying assumptions. We compare their performance on simulated collider data.

1. Introduction. The Standard Model (SM) of particle physics is a theory describing the interactions between elementary particles—the building blocks of matter. One key component of the SM is the presumed existence of a quantum field responsible for generating mass in certain elementary particles. This field is known as the Higgs field, originally theorized by Higgs (1964), Englert and Brout (1964). Excitations of the Higgs field produce particles, known as Higgs bosons, which were the subject of an intensive search by experimental particle physicists ever since the mid 1970s. In July 2012, two independent experiments at the Large Hadron Collider (LHC) at CERN (the European Organization for Nuclear Research) announced the observation of a new particle consistent with the SM Higgs boson (ATLAS, 2012; CMS, 2012). Having discovered this Higgs-like particle, current work is concerned with detailed studies of its properties, in order to confirm or refute those predicted by the SM. One such property is the so-called Higgs boson *self-coupling*, whereby a single excitation of the Higgs field can split into two Higgs bosons without intermediate interactions

MSC2020 subject classifications: Primary 62P35; secondary 62G05,62M45,62M09.

Keywords and phrases: High Energy Physics, Large Hadron Collider, Optimal Transport Map, Wasserstein Distance, Domain Adaptation, Transfer Learning, Residual Neural Network.

with other particles. Observing this phenomenon would provide compelling new information regarding the mechanism of particle mass generation. This paper is concerned with some of the statistical challenges posed by such a measurement.

The LHC is housed in a massive underground tunnel in which two counter-rotating beams of protons are accelerated to nearly the speed of light. When these protons collide, new particles are almost always formed, and their paths within particle detectors are recorded. Individual collisions are known as *events*. An event in which two Higgs bosons are generated is called a *double Higgs (or di-Higgs) event*. The Higgs boson is a highly unstable particle, thus whenever it is produced, it decays into other particles almost immediately, making di-Higgs production impossible to observe directly.

The Higgs boson most commonly decays into a pair of so-called bottom quarks (*b*-quarks). An event in which four *b*-quarks are observed is thus a candidate di-Higgs event, but could also have arisen from various other physical processes that produce four *b*-quarks. We say that a di-Higgs event in which the Higgs bosons decay into four *b*-quarks is a *signal event*, while any other event tagged as having four *b*-quarks is called a *background event*. The problem of searching for double Higgs boson production reduces to testing whether the proportion of signal events is nonzero among the observed data. As we describe in Section 3, carrying out this test is a well-understood statistical task when the distribution of both background and signal events is known. While the di-Higgs signal distribution can be approximated to sufficient accuracy with first-principles simulation, simulating the background distribution suffers from large high-order corrections which are computationally intractable (Di Micco et al., 2020). Instead, the background distribution must be estimated using the observed data. This is known as the problem of *data-driven background modeling*, which is the main subject of this paper.

As stated, the background distribution is not a statistically identifiable quantity, due to the potential presence of an unknown proportion of signal in the data. Any analysis strategy must therefore make some modeling assumptions to make the background estimation problem tractable. As we discuss below, it is standard to assume that the background distribution is related in some way to the distribution of certain *auxiliary events*, which in turn is identifiable. An example of useful auxiliary events is those consisting of less than four observed *b*-quarks, since they are unlikely to be signal events, but are kinematically related to $4b$ background events (Bryant, 2018). Stated differently, the distribution of appropriately chosen auxiliary events is an identifiable estimand which has undergone a *distributional shift* relative to the non-identifiable background distribution of interest. If the analyst has access to a sample of auxiliary events, its empirical distribution provides a first naive approximation of the desired background distribution. To obtain a more precise estimate, one must correct for the distributional shift and cross-check the assumptions used to do so.

1.1. *Our Contributions.* This paper develops two methodologies for data-driven background modeling in di-Higgs boson searches. Our methods are fully nonparametric, and each hinge upon a characteristic modeling assumption. The assumptions made by our methods are distinct and complementary, thus these methods can serve as cross-checks for each other in di-Higgs boson searches, an important benefit that will increase the analyst’s trust in the obtained background estimates.

Our first approach develops a probabilistic classifier for discriminating auxiliary events from background events. This classifier leads to an estimate of the *density ratio* between such events. We fit this density ratio in a signal-free region of the phase space, known as the *Control Region*, and then extrapolate it to the region of primary interest, known as the *Signal Region*. Any deviation of this extrapolated density ratio from unity is then used to correct the distributional shift undergone by the auxiliary sample. As we discuss in Section 1.2, variants

of this procedure are the most widely-used approach to data-driven background modeling; our contribution here is to develop a powerful new classifier for this method, which is specifically tailored to collider data. In particular, our classifier is a convolutional neural network with residual layers (He et al., 2016), whose architecture accounts for the structure and symmetries of collider events with multiple identical final state objects.

Our second contribution is to develop a new background estimation method which is based on the optimal transport problem between distributions of collider events. Optimal transport has already proven to be a powerful tool for unsupervised domain adaptation in classification problems (Courty et al., 2016), and here we propose to use it rather differently to correct distributional shifts between estimates of the auxiliary and background distributions. Our approach involves the out-of-sample estimation of optimal transport maps, for which we consider two different estimators. While the first is based on smoothing of an in-sample optimal coupling, and has previously been proposed in the literature (cf. Section 1.2), our second estimator appears to be new, and also leverages our new classifier for collider data.

The optimal transport problem requires a metric on the space of collider events, for which we employ a variant of the metric proposed by Komiske, Metodiev and Thaler (2019), which is itself obtained through the optimal transport problem of matching clusters of energy deposits in collision events. Our approach therefore involves a nested use of optimal transport.

We illustrate the empirical performance of our two methodologies on realistic simulated collider data. We observe that both approaches lead to quantitatively similar background estimates, despite the complementarity of their underlying modeling assumptions. In particular, this example illustrates how our methods can be used to cross check each other in practice.

1.2. Related Work. Di-Higgs boson production has been the subject of numerous recent searches by the ATLAS and CMS collaborations at the LHC—we refer to the recent survey paper of Di Micco et al. (2020) for an overview. The four b -quark final state is the most common decay channel for di-Higgs events, but suffers from a large multijet background as described previously. Each of the most recent searches in this final state (e.g. ATLAS (2018a), ATLAS (2019), ATLAS (2021), CMS (2022), ATLAS) performed data-driven background estimation by first estimating a density ratio (between background and auxiliary events) in a Control Region, and extrapolating this density ratio to the Signal Region. Certain searches, such as ATLAS (2019), estimate the density ratio using heuristic one-dimensional reweighting schemes, while others, such as CMS (2022), use off-the-shelf multivariate classifiers for this purpose. Our work builds upon the latter approach by designing a classifier tailored to the structure and symmetries present in collider data.

The idea of estimating density ratios using classifiers has a long history in statistics—see for instance Qin (1998), Cheng and Chu (2004), Kpotufe (2017)—and appears in a variety of applications in experimental particle physics (e.g. Cranmer, Pavez and Louppe (2015), Brehmer et al. (2020), CMS (2022)). Classification-based estimators have the practical advantage of circumventing the need for high-dimensional density estimation, which can be particularly challenging to perform over the space of collider events. In the context of background estimation, a density ratio is first estimated in the Control Region, and then extrapolated into the Signal Region; this extrapolation can be viewed as an instance of *transfer learning* (Weiss, Khoshgoftaar and Wang, 2016). It has been empirically witnessed that modern classification algorithms, such as deep neural networks, have the ability to transfer well to new distributions (Yosinski et al., 2014), which further motivates their use for density ratio estimation in the context of background estimation.

While a careful choice of classifier can greatly improve the accuracy of transfer learning, such a transfer cannot be possible if the underlying distribution in the Signal Region is unconstrained relative to its counterpart in the Control Region. Therefore, this type of procedure must necessarily place an implicit modeling assumption on the underlying distributions,

which is typically difficult to verify in practice. Given that variants of this procedure are used in each of the most recent di-Higgs searches listed above, this motivates us to develop a background estimation method with a complementary modeling assumption, in Section 5. Rather than density ratios, the key object of interest in this methodology will be the notion of an *optimal transport map*, which arises from the celebrated optimal transport problem (Villani, 2003). Optimal transport has received a surge of recent interest in the statistics and machine learning literature—we refer to Panaretos and Zemel (2019a,b); Kolouri et al. (2017); Peyré and Cuturi (2019) for recent reviews. Closest to our setting are recent applications of optimal transport to domain adaptation for classification problems; see for instance Courty et al. (2016), Redko, Habrard and Sebban (2017), Rakotomamonjy et al. (2022), and references therein. Nested optimal transport formulations, as in our work, have recently been used for other tasks such as multilevel clustering (Ho et al., 2017, 2019; Huynh et al., 2021) and multimodal distribution alignment (Lee et al., 2019).

Our methodology relies on the estimation of optimal transport maps or couplings between distributions of collider events. The question of estimating optimal transport maps over Euclidean space has been the subject of intensive recent study (Perrot et al., 2016; Forrow et al., 2018; Makuva et al., 2019; Schiebinger et al., 2019; Nath and Jawanpuria, 2020; Hütter and Rigollet, 2021; de Lara, González-Sanz and Loubes, 2021; Deb, Ghosal and Sen, 2021; Manole et al., 2021; Ghosal and Sen, 2022; Gunsilius, 2022). While many of these works are tailored to the quadratic cost function, the widely-used nearest-neighbor estimator (Flamary et al., 2021; Manole et al., 2021) can naturally be defined over the non-Euclidean ground space appearing in our work, and is used in one of our background estimators defined in Section 5.2.2.

Beyond the search of di-Higgs boson production, we emphasize that the question of background estimation arises in a variety of problems in experimental high-energy physics, where our methodologies could also potentially be applied. We refer to the book of Behnke et al. (2013) for a pedagogical introduction to statistical aspects of the subject; see also Appendix 1 of Lyons (1989). Finally, we mention some recent advances on the widely-used sPlot (Barlow, 1987; Pivk and Le Diberder, 2005; Borisov and Kazeev, 2019; Dembinski et al., 2022) and ABCD (Alison, 2015; Aad et al., 2015; Choi and Oh, 2021; Kasieczka et al., 2021) techniques for background estimation, the latter of which can be viewed as a precursor to the methods developed in this paper.

1.3. *Paper Outline.* The rest of this paper is organized as follows. Section 2 contains background about the LHC and di-Higgs boson production. Section 3 outlines the statistical procedure used for signal searches in collider experiments at the LHC, and mathematically formulates the data-driven background modeling problem. In Section 4, we describe how to perform background estimation using a classifier for discriminating auxiliary events from background events, and we describe our new classifier architecture for this purpose. In Section 5, we describe a new approach to background modeling based on the optimal transport problem. We then compare these methods in a simulated di-Higgs search in Section 6. We close with a discussion in Section 7.

2. Background.

2.1. *LHC Experiments and di-Higgs Boson Production.* The LHC is the largest particle collider in the world, consisting of a 27 kilometer-long tunnel in which two counter-rotating beams of protons are accelerated to nearly the speed of light. These particles are primarily collided in one of four underground detectors, named ALICE, ATLAS, CMS and LHCb. ATLAS and CMS are general-purpose detectors used for a wide range of physics analyses,

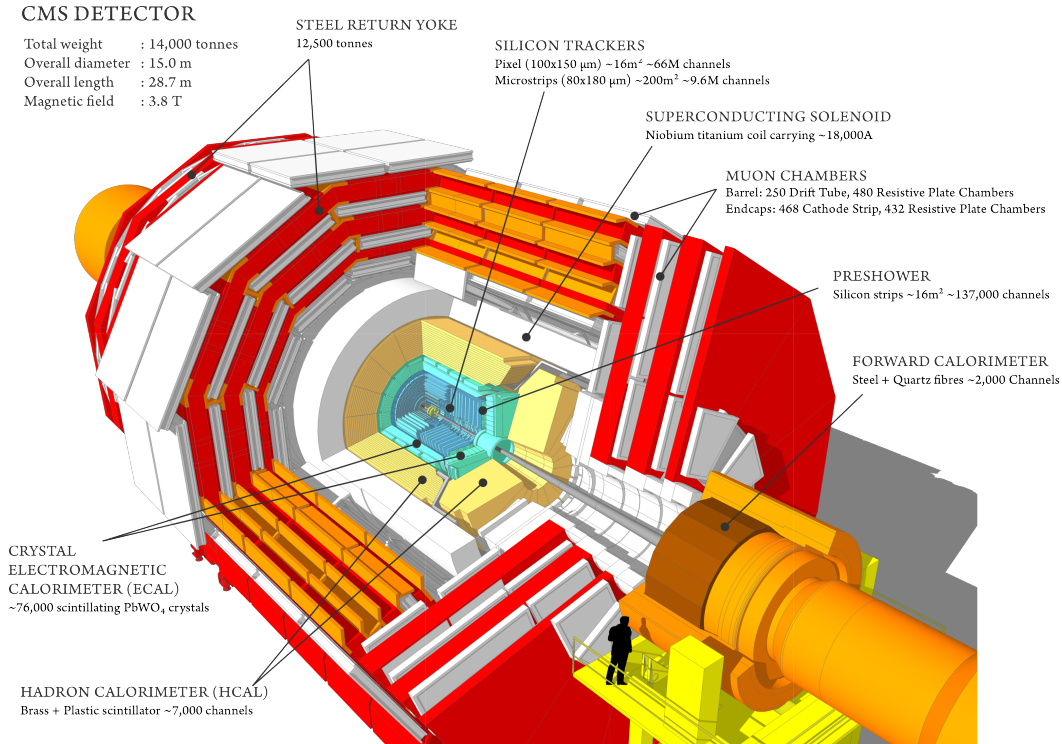


FIG 1. Illustration of the CMS detector (Sakuma and McCauley, 2014). Counter-rotating beams of protons are made to collide in the center of the detector. The trajectory and mass of each particle emanating from the collision is then recorded.

including Higgs boson-related searches, while ALICE and LHCb focus on specific physics phenomena. We focus on the CMS detector in what follows, but similar descriptions can be made for the ATLAS detector.

When two protons collide, their energy is converted into matter, in the form of new particles. The goal of the CMS (Compact Muon Solenoid) detector is to measure the momenta, energies and types of such particles. To measure their momenta, CMS is built around a giant superconducting solenoid magnet, depicted in Figure 1, which deforms the trajectories of particles as they move from the center of the detector outward through a silicon tracker. The extent to which the trajectory of a charged particle is bent depends on its momentum and can hence be used to measure the momentum. After the silicon tracker, CMS consists of several layers of calorimeters which measure the energies of the particles. We refer to CMS (2008) for a complete description of the CMS detector.

Certain proton-proton collisions give rise to highly unstable particles which decay almost instantly into more stable particles. In this case, the detector is only able to observe these long-lived particles. By measuring their energies and momenta, insight can be gained into the physical properties of the unstable particles from which they originate.

The Higgs boson is an example of an unstable particle, which decays within approximately 10^{-22} seconds. The SM predicts that a Higgs boson decays into a pair of bottom quarks (b -quarks) 60% of the time, and this decay channel has indeed been observed experimentally (ATLAS, 2018b; CMS, 2018a). Other channels which have been observed experimentally include the decay of a Higgs boson into pairs of photons (ATLAS, 2018c; CMS, 2018b), W bosons (ATLAS, 2018d; CMS, 2019), Z bosons (ATLAS, 2018e; CMS, 2018c), and tau

leptons (; CMS, 2018d). The SM further predicts the rare possibility that two Higgs bosons can be produced simultaneously, and this paper is concerned with the statistical challenges arising in the search for this process, which has yet to be observed experimentally. If this process were to occur, the two resulting Higgs bosons would each, in turn, be most likely to decay into two b -quarks, thus making four b -quarks the most common final state of di-Higgs boson events. We focus on this decay channel (abbreviated $\text{HH} \rightarrow 4b$) throughout this paper. We note that b -quarks form into bound states with other quarks called b -hadrons which are themselves unstable, and rapidly decay into collimated sprays of stable particles called b -jets, which can be efficiently identified by the CMS detector.

2.2. Collider Events and the CMS Coordinate System. Particles measured by the CMS detector are typically represented in spherical coordinates. Given a particle with momentum vector $v = (x, y, z) \in \mathbb{R}^3$, its azimuthal angle $\phi \in [0, 2\pi)$ is defined as the angle increasing from the positive x -axis to the positive y -axis, while the polar angle $\theta \in [0, \pi)$ is increasing from the positive z -axis to the positive y -axis. The length of its projection onto the (x, y) plane is called the *transverse momentum* p_T . It is common to replace the polar angle θ by the *pseudorapidity* of the particle, given by $\eta = -\log(\tan(\theta/2))$.

In addition to the variables p_T, η and ϕ , the rest mass m of each particle can be obtained from the energy measurements made by the calorimeters in the CMS detector. Altogether, a particle jet is analyzed as a single point in this coordinate system, and encoded as a four-dimensional vector (p_T, η, ϕ, m) . In our search channel, collisions lead to multiple, say $K \geq 1$, jets measured by the detector, which may be encoded as the $4K$ -dimensional vector $(p_{T_i}, \eta_i, \phi_i, m_i : 1 \leq i \leq K)$. We opt for an alternative notation, which will be particularly fruitful for the purpose of defining a metric between collider events in Section 5.3. Specifically, an event will henceforth be represented by the discrete measure

$$(2.1) \quad g = \sum_{i=1}^K p_{T_i} \delta_{(\eta_i, \phi_i, m_i)},$$

where δ_x denotes the Dirac measure placing unit mass at a point $x \in \mathbb{R}^3$. In particular, the representation (2.1) emphasizes the invariance of an event with respect to the ordering of its jets. The transverse momenta p_{T_i} may be viewed as a proxy for the energy of each jet, thus the total measure of g denotes its total energy, denoted $s_T = \sum_{i=1}^K p_{T_i}$. The set of events with K jets of interest is denoted by

$$\mathcal{G}^{(K)} = \left\{ \sum_{j=1}^K p_{T_j} \delta_{(\eta_j, \phi_j, m_j)} : p_{T_j}, m_j > 0, \phi_j, \eta_j \in \mathbb{R}, 1 \leq j \leq K \right\},$$

where the definition of ϕ_j is extended from $[0, 2\pi)$ to the entire real line by 2π -periodicity. In the context of double Higgs boson production in the four b -jet final state, the choice $K = 4$ will be most frequently used, and in this case we simply write $\mathcal{G} = \mathcal{G}^{(4)}$.

Finally, we note that events are deemed invariant under the orientation of the x - and z -axes. This fact, together with the periodicity of the angle ϕ , implies that two events $g = \sum_{j=1}^K p_{T_j} \delta_{(\eta_j, \phi_j, m_j)} \in \mathcal{G}^{(K)}$ and $g' = \sum_{j=1}^K p'_{T_j} \delta_{(\eta'_j, \phi'_j, m'_j)} \in \mathcal{G}^{(K)}$ may be deemed equivalent if they are mirror-symmetric in η, ϕ , as well as rotationally symmetric in ϕ , that is, if there exist $\Delta \in [0, 2\pi)$ and $\iota_1, \iota_2 \in \{-1, 1\}$ such that

$$(2.2) \quad \sum_{j=1}^K p_{T_j} \delta_{(\iota_1 \eta_j, \Delta + \iota_2 \phi_j, m_j)} = \sum_{j=1}^K p'_{T_j} \delta_{(\eta'_j, \phi'_j, m'_j)}.$$

Formally, we define an equivalence relation \simeq between events in $\mathcal{G}^{(K)}$, such that $g \simeq g'$ if and only if there exist Δ, ι_1, ι_2 for which (2.2) holds.

3. Problem Formulation.

3.1. *Overview of Signal Searches at the LHC.* In order to make inferences about the presence or absence of a signal process in collider data, event counts are commonly analyzed as binned Poisson point processes. While we focus on the setting of double Higgs boson production in the four b -quark final state, the description that follows is representative of a wide range of signal searches for high-energy physics experiments.

Let ν_0 denote a σ -finite Borel measure over the state space \mathcal{G} of collider events, with respect to a fixed choice of Borel σ -algebra on \mathcal{G} denoted $\mathbb{B}(\mathcal{G})$. Let F denote an inhomogeneous Poisson point process (Reiss, 2012) with a nonnegative intensity function $f \in L^2(\mathcal{G})$ on \mathcal{G} , that is, F is a random point measure on \mathcal{G} such that

1. $F(B) \sim \text{Poisson}(\lambda(B))$, where λ is the intensity measure induced by f , defined by $\lambda(B) = \int_B f d\nu_0$ for all $B \in \mathbb{B}(\mathcal{G})$;
2. $F(O_1), \dots, F(O_\ell)$ are independent for all pairwise disjoint sets $O_1, \dots, O_\ell \in \mathbb{B}(\mathcal{G})$, for all integers $\ell \geq 1$.

Every four b -jet collision event is either a *signal event*, namely an event arising from two Higgs bosons, or a *background event*, arising from some other physical process. Letting $\mu \geq 0$ denote the rate of signal events, we write the intensity measure λ as

$$\lambda(B) = \beta_4(B) + \mu\sigma(B), \quad B \in \mathbb{B}(\mathcal{G}),$$

where β_4 and σ , respectively, denote nonnegative background and signal intensity measures. σ is typically normalized such that the value $\mu = 1$ corresponds to the theoretical prediction of the signal rate. The measures β_4 and σ typically depend on nuisance parameters related to the calibration of the detector, the uncertain parameters of certain physical processes, such as the parton distribution functions of the proton (Placakyte, 2011), and so on. We suppress the dependence on such nuisance parameters for ease of exposition. The parameter μ is of primary interest, since non-zero values of μ indicate the existence of signal events. A search for the signal process therefore reduces to testing the following hypotheses on the basis of observations from the Poisson point process F :

$$(3.1) \quad H_0 : \mu = 0 \quad \text{vs.} \quad H_1 : \mu > 0.$$

Given a sequence G_1, G_2, \dots of observed events, we may write $F = \sum_{i=1}^M \delta_{G_i}$, where $M \sim \text{Poisson}(\lambda(\mathcal{G}))$ is independent of the observations, which satisfy

$$(3.2) \quad G_1, G_2, \dots \stackrel{\text{iid}}{\sim} \frac{\lambda}{\lambda(\mathcal{G})} = \epsilon S + (1 - \epsilon)P_4.$$

Here, $S = \sigma/\sigma(\mathcal{G})$ and $P_4 = \beta_4/\beta_4(\mathcal{G})$ denote the respective signal and background distributions, and $\epsilon = \mu\sigma(\mathcal{G})/\lambda(\mathcal{G})$ the proportion of signal events.

The Poisson point process F is often binned in practice. Let $h : \mathcal{G} \rightarrow \mathcal{A} \subseteq \mathbb{R}$ denote a dimensionality reduction map, to be discussed below, which will be used to bin the point process using univariate bins. Let $\{I_j\}_{j=1}^J$ denote a collection of bins forming a partition of \mathcal{A} , and define the event counts

$$(3.3) \quad D_j = F(h^{-1}(I_j)) = |\{1 \leq i \leq M : h(G_i) \in I_j\}|, \quad j = 1, \dots, J.$$

The definition of F implies that the random variables D_j are independent and satisfy

$$(3.4) \quad D_j \sim \text{Poisson}(B_j + \mu S_j), \quad j = 1, \dots, J,$$

where $B_j = \beta_4(h^{-1}(I_j))$ and $S_j = \sigma(h^{-1}(I_j))$.

The likelihood ratio test with respect to the joint distribution of D_1, \dots, D_J is typically used to test the hypotheses (3.1) (ATLAS, CMS and Higgs Combination Group, 2011). The binned likelihood function for the parameter μ is given by

$$(3.5) \quad L(\mu) = \prod_{j=1}^J \frac{(B_j + \mu S_j)^{D_j}}{D_j!} e^{-(B_j + \mu S_j)}.$$

Di-Higgs events are rare in comparison to background events, thus the signal-to-background ratio is low. At the time of writing, values of M which are typically observed at the LHC may be too small for any test to have power in rejecting the null hypothesis in (3.1) at desired significance levels. Analyses which fail to reject H_0 instead culminate in an upper confidence bound on μ , also known as an upper limit (ATLAS, CMS and Higgs Combination Group, 2011).

The power of the likelihood ratio test for (3.1) may be increased by choosing a function h which maximizes the separation between background and signal event counts across the J bins. Informally, the optimal such choice of h is given by

$$(3.6) \quad h(g) = \mathbb{P}(G \text{ is a Signal Event} | G = g),$$

which may be estimated using a multivariate classifier, such as a neural network or boosted decision trees, for discriminating background events from signal events.

The signal intensity measure σ is theoretically predicted by the SM, and can be approximated well using Monte Carlo event generators (Di Micco et al., 2020). The background intensity β_4 is, however, intractable due to the strongly interacting nature of quantum chromodynamics (QCD) in which events with the four b -quark final state can be produced via an enormous number of relevant and complex pathways. The intensity measure β_4 , or its binned analogue $(B_j)_{j=1}^J$, must therefore be estimated from the collider data itself, which we refer to as *data-driven background modeling*. This problem constitutes the primary focus of this paper.

3.2. Setup for Data-Driven Background Modeling. The aim of this paper is to develop data-driven estimators of the background intensity measure β_4 . The primary challenge is the fact that the sample G_1, \dots, G_M is contaminated with an unknown proportion ϵ of signal events. The background estimation problem is thus statistically unidentifiable as stated, and it will be necessary to impose further modeling assumptions.

In order to formulate these assumptions and our resulting background modeling methods, we assume that the analyst has access to a second Poisson Point Process $T = \sum_{i=1}^N \delta_{H_i}$ consisting of auxiliary events which were tagged by the CMS detector as having four jets, of which exactly three are b -jets. We refer to such events as “ $3b$ events”, as opposed to “ $4b$ events” which were identified as having four b -jets. We stress that the terms $3b$ and $4b$ do not refer to the true number of b -quarks arising from the collision, rather the number of b -jets identified by the detector¹. As we further discuss in Section 6, the majority of $3b$ events in fact arise from the hadronization of two b -quarks and two charm or light quarks, while a small proportion arise from four b -quarks. For the purpose of a discovery analysis, the $3b$ sample H_1, H_2, \dots, H_N can therefore be treated as having a negligible proportion of signal events (Bryant, 2018; CMS, 2022). We treat this proportion as zero for sake of exposition. We shall henceforth denote the intensity measure of the point process T by β_3 , and we denote by $P_3 = \beta_3 / \beta_3(\mathcal{G})$ the corresponding probability distribution of the independent observations H_1, H_2, \dots .

¹An event with exactly three b -quarks is not physical, since b -quarks can only arise in pairs; however, the detector may incorrectly label events as having three b -jets.

The kinematics of the 3b events are expected to be similar, but not equal, to those of 4b background events (CMS, 2022). However, unlike β_4 , notice that β_3 is an identifiable estimand, due to the lack of signal events in the 3b process T . Any consistent estimator $\widehat{\beta}_3$ of this quantity can be used to provide a zeroth-order approximation of β_4 (up to a correction for normalization). This approximation is, however, insufficiently accurate to be used as a final estimate of β_4 and our goal is to develop statistical methods for correcting this naive background estimate.

Recall that the four b -jets of any signal event $g \in \mathcal{G}$ are naturally paired, with each pair arising from a Higgs boson. The true pairing of the jets is unknown to the detector; however, it may be approximated, for instance using an algorithm due to Bryant (2018). We use the same pairing algorithm in our work. Given as input an event g , this deterministic algorithm outputs one among the three distinct unordered pairs of measures $\{g^1, g^2\} \subseteq \mathcal{G}^{(2)}$ which satisfy $g = g^1 + g^2$. We refer to g^1 and g^2 as *dijets*. When g is a signal event, we expect that each dijet arose from a decay of a Higgs boson, whereas when g is a background event, we expect that at least one of the two dijets arose from the decay of a different particle.

The Higgs boson is known to have mass m_H approximately equal to 125 GeV (ATLAS, 2012; CMS, 2012). It follows that the two dijets should approximately satisfy $m(g^1) \approx m(g^2) \approx m_H$, where $m(a)$ denotes the invariant mass² of any $a \in \mathcal{G}^{(K)}$, $K \geq 1$. Large deviations of the dijet invariant masses from 125 GeV indicate that g is not a signal event. This provides a heuristic for determining events among G_1, \dots, G_M which are unlikely to be signal events. To this end, we form subsets $\mathcal{G}_c, \mathcal{G}_s \subseteq \mathcal{G}$ such that $\mathcal{G}_c \cap \mathcal{G}_s = \emptyset$, where \mathcal{G}_s is called the *Signal Region*, containing events with dijet masses near m_H , and \mathcal{G}_c is called the *Control Region*, containing all other events which will be used in the analysis. We follow Bryant (2018) and employ the following specific definitions of \mathcal{G}_c and \mathcal{G}_s :

$$(3.7) \quad \mathcal{G}_s = \left\{ g \in \mathcal{G} : \sqrt{\left(1 - \frac{m_H}{m(g^1)}\right)^2 + \left(1 - \frac{m_H}{m(g^2)}\right)^2} \leq \kappa_s \right\},$$

$$(3.8) \quad \mathcal{G}_c = \left\{ g \in \mathcal{G} : \sqrt{\left(m(g^1) - \sigma_C m_H\right)^2 + \left(m(g^2) - \sigma_C m_H\right)^2} \leq \kappa_c \right\} \setminus \mathcal{G}_s,$$

for some constants $\sigma_c, \kappa_c, \kappa_s > 0$. These regions are illustrated in Figure 2 for a simulated background sample. We similarly partition the Poisson intensity measures β_3, β_4 , by defining for all $B \in \mathbb{B}(\mathcal{G})$,

$$\beta_j^c(B) = \beta_j(B \cap \mathcal{G}_c), \quad \beta_j^s(B) = \beta_j(B \cap \mathcal{G}_s), \quad j = 3, 4.$$

These four measures are illustrated in Figure 3. Furthermore, we assume for ease of exposition that these measures are absolutely continuous with respect to the dominating measure ν_0 , and we let $b_j^a = d\beta_j^a/d\nu_0$ for all $j = 3, 4$ and $a = c, s$.

Recall that the collider events associated with the intensity measures β_3^c and β_3^s are signal-free by construction, and those from β_4^c are also signal-free under the assumption that negligibly few signal events will fall outside of \mathcal{G}_s . These three intensity measures can therefore be estimated directly by means of their empirical intensity functions. We have thus reduced the background modeling problem to that of estimating β_4^s , given estimates of β_3^c, β_3^s and β_4^c .

²If E denotes the sum of the energies of the constituent jets of a , and p denotes the magnitude of the sum of their momentum vectors, then the invariant mass of e is defined by $m(a) = \sqrt{E^2 - p^2}$ (Hagedorn, 1964; Martin and Shaw, 2017).

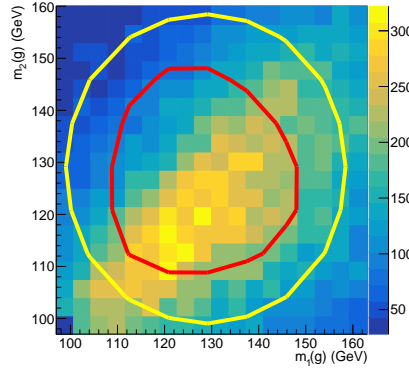


FIG 2. Illustration of the Control and Signal Regions. The two-dimensional histogram represents simulated 4b collider events described in Section 6, plotted in terms of their dijet invariant masses. We emphasize that this is a low-dimensional representation; the events considered in this work are 16-dimensional. The red line indicates the boundary of the Signal Region, while the annulus bounded by the yellow line represents the Control Region. The constants σ_c, κ_c and κ_s used in this figure are stated in Section 6.

To this end, we will partition the samples into the sets

$$\begin{aligned} \{G_1^s, \dots, G_{m_s}^s\} &:= \{G_1, \dots, G_M\} \cap \mathcal{G}_s, & \{H_1^s, \dots, H_{n_s}^s\} &:= \{H_1, \dots, H_N\} \cap \mathcal{G}_s, \\ \{G_1^c, \dots, G_{m_c}^c\} &:= \{G_1, \dots, G_M\} \cap \mathcal{G}_c, & \{H_1^c, \dots, H_{n_c}^c\} &:= \{H_1, \dots, H_N\} \cap \mathcal{G}_c, \end{aligned}$$

where $M = m_c + m_s$ and $N = n_c + n_s$. Furthermore, let

$$\beta_{3,n_c}^c = T|_{\mathcal{G}_c} = \sum_{i=1}^{n_c} \delta_{H_i^c}, \quad \beta_{3,n_s}^s = T|_{\mathcal{G}_s} = \sum_{i=1}^{n_s} \delta_{H_i^s}, \quad \beta_{4,m_c}^c = F|_{\mathcal{G}_c} = \sum_{i=1}^{m_c} \delta_{G_i^c}$$

denote the empirical estimators of the measures $\beta_3^c, \beta_3^s, \beta_4^c$, illustrated in the background of Figure 3. As previously noted, the measure β_3^s provides a zeroth-order approximation of β_4^s (after a normalization correction), thus a naive first estimate of β_4^s is given by β_{3,n_s}^s . As we shall see in the simulation study of Section 6, this approximation is insufficiently accurate to be used as a final estimator. Our methodologies improve upon it by modeling the discrepancy between the 3b and 4b distributions in the Control Region via $\beta_{4,m_c}^c, \beta_{3,n_c}^c$, and then making use of that information in the Signal Region to improve the accuracy of β_{3,n_s}^s as an estimator of β_4^s .

Once we are able to derive an estimator $\hat{\beta}_4^s$ of β_4^s , based on the signal-free observations $G_1^c, \dots, G_{m_c}^c, H_1^s, \dots, H_{n_s}^s, H_1^c, \dots, H_{n_c}^c$, we may define the fitted histogram $\hat{B}_j = \hat{\beta}_4^s(h^{-1}(I_j))$, $j = 1, \dots, J$. One may then test the hypotheses (3.1) using the likelihood ratio test, based on the following modification of the likelihood function in equation (3.5),

$$(3.9) \quad \tilde{L}(\mu) = \prod_{j=1}^J \frac{(\hat{B}_j + \mu S_j)^{D_j^s}}{D_j^s!} e^{-(\hat{B}_j + \mu S_j)}, \quad \text{where } D_j^s = |\{1 \leq i \leq m_s : h(G_i^s) \in I_j\}|.$$

Here, \tilde{L} can be viewed as a restriction of the likelihood L to the Signal Region. Notice that \hat{B}_j is independent of D_k^s , for any j, k . In practice, it is also necessary to incorporate statistical and systematic uncertainties pertaining to the estimator \hat{B}_j into the hypothesis testing procedure (ATLAS, CMS and Higgs Combination Group, 2011). Since formal uncertainty

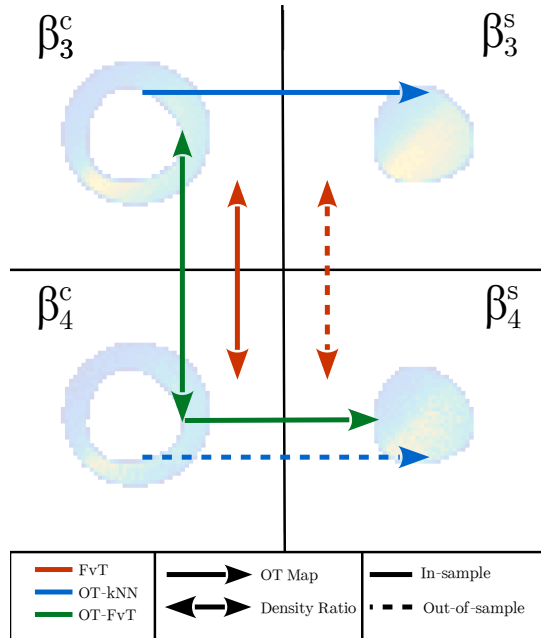


FIG 3. Illustration of the four Poisson intensity measures $\beta_3^C, \beta_3^S, \beta_4^C, \beta_4^S$, among which only the latter is nontrivial to estimate, and summary of the three methods developed in this paper for estimating β_4^S . The method FvT (Four vs. Three) estimates the ratio of the two densities in the Control Region using a classifier, and then extrapolates it into the Signal Region using out-of-sample evaluations of the classifier. The OT-kNN (Optimal Transport-k Nearest Neighbors) method produces an estimator \hat{T} of the optimal transport map T between the 3b Control and Signal Region distributions, and evaluates this estimator out-of-sample on an estimator of the 4b Control Region distribution. The out-of-sample evaluation of \hat{T} is performed using nearest-neighbor extrapolation. The OT-FvT (Optimal Transport-Four vs. Three) method combines these ideas: first, it uses the classifier to produce an estimator of β_4^C with the same support as β_{3,n_c}^C , and second, it pushes forward this estimator through \hat{T} , thereby avoiding out-of-sample evaluations of both the classifier and optimal transport map. The background of the figure consists of bivariate histograms of simulated 3b and 4b samples in the Control and Signal Regions, plotted in terms of their dijet invariant masses, as in Figure 2.

quantification for background modeling is beyond the scope of this work, we omit further details, and provide further discussion of this point in Section 7. With this framework in place, the primary difficulty remaining in the testing problem (3.1) is that of deriving estimators of the background intensity measure β_4^S . In what follows, we derive three estimators for this quantity, outlined in Figure 3, which rely on complementary modeling assumptions.

4. Background Modeling via Density Ratio Extrapolation. The discrepancy between 3b and 4b background distributions may be directly quantified in the Control Region, where no signal events are present. Under the assumption that these distributions vary sufficiently smoothly between the Control and Signal Regions, this discrepancy may be extrapolated into the signal region to produce a correction of the 3b signal region intensity measure β_3^S , leading to an estimate of β_4^S . This general strategy forms the basis of most existing background modeling methodologies discussed in Section 1.2. We first recall in this section how this approach may be carried out using a classifier for discriminating 3b and 4b events. We then develop a new classifier architecture specifically tailored to this type of collider data. Beyond its use for background modeling, this classifier will make a reappearance in Section 6, where we use it as a tool for validating fitted background models. We will also employ the same classifier

architecture for discriminating background and signal events, and ultimately use it as the final binning function in equation (3.6).

4.1. *Reduction to Classification.* Let G denote a random collider event, arising from either the $3b$ or $4b$ distributions, and define the latent binary random variable Z indicating the component membership of G ; that is, Z takes on the value 1 if G is $4b$ and takes on the value 0 if G is $3b$. Setting $\psi(g) = \mathbb{P}(Z = 1|G = g)$, it is a straightforward consequence of Bayes Rule that

$$(4.1) \quad \frac{b_4^c(g)}{b_3^c(g)} = \frac{\psi(g)}{1 - \psi(g)}, \quad g \in \mathcal{G}_c,$$

and hence,

$$(4.2) \quad \beta_4^c(B) = \int_B \frac{\psi(g)}{1 - \psi(g)} d\beta_3^c(g), \quad B \in \mathbb{B}(\mathcal{G}_c).$$

Equations (4.1–4.2) are a reformulation for our context of the well-known fact that, up to normalization, a likelihood ratio may be expressed as an odds ratio (cf. Section 1.2). Estimating the ratio of $3b$ to $4b$ intensity functions in the Control Region thus reduces to the classification problem of estimating ψ , say by a classifier $\hat{\psi}$. This observation has the practical advantage of circumventing the need of performing high-dimensional density estimation. Assuming that the estimator $\hat{\psi}$ can be evaluated in the Signal Region \mathcal{G}_s , disjoint from its training region \mathcal{G}_c , we may postulate that the measure

$$(4.3) \quad B \in \mathbb{B}(\mathcal{G}_s) \mapsto \int_B \frac{\hat{\psi}(g)}{1 - \hat{\psi}(g)} d\beta_3^s(g),$$

provides a reasonable approximation of β_4^s . The quality of such an approximation is driven by the ability of the classifier $\hat{\psi}$ to generalize between regions of the phase space. To formalize this, we will assume for simplicity that $\hat{\psi}$ is a parametric classifier lying in a class $\{\psi_\alpha : \mathcal{G} \rightarrow [0, 1] : \alpha \in \Omega\}$, for some parameter space $\Omega \subseteq \mathbb{R}^d$, $d \geq 1$, which is obtained via the minimization problem

$$\hat{\psi} = \psi_{\hat{\alpha}}, \quad \text{where } \hat{\alpha} \in \operatorname{argmin}_{\alpha \in \Omega} \left\{ \frac{1}{n_c} \sum_{i=1}^{n_c} \mathcal{L}(\psi_\alpha(H_i^c), 0) + \frac{1}{m_c} \sum_{j=1}^{m_c} \mathcal{L}(\psi_\alpha(G_j^c), 1) \right\},$$

for a loss function $\mathcal{L} : [0, 1]^2 \rightarrow \mathbb{R}$. We then make the following assumption.

ASSUMPTION 1. *The conditional probability ψ satisfies the following conditions.*

- (i) (*Correct Specification*) *There exists $\alpha^* \in \Omega$ such that $\psi = \psi_{\alpha^*}$.*
- (ii) (*Generalization*) *We have,*

$$\alpha^* \in \operatorname{argmin}_{\alpha \in \Omega} \mathbb{E}[\mathcal{L}(\psi_\alpha(G), Z)|G \in \mathcal{G}_c].$$

Assumption 1 implies that a classifier trained solely in the Control Region can consistently estimate the full conditional probability $\psi(g)$, for events $g \in \mathcal{G}$ lying in both the Control and Signal Regions. Such an assumption guarantees the ability of the classifier $\hat{\psi}$ to generalize from the Control Region, making the ansatz (4.3) justified. A natural estimator for β_4^s is then obtained by replacing β_3^s in equation (4.3) by its empirical counterpart β_{3,n_s}^s . Doing so leads to the estimator

$$\hat{\beta}_4^s = \sum_{i=1}^{n_s} \frac{\hat{\psi}(H_i^s)}{1 - \hat{\psi}(H_i^s)} \delta_{H_i^s}.$$

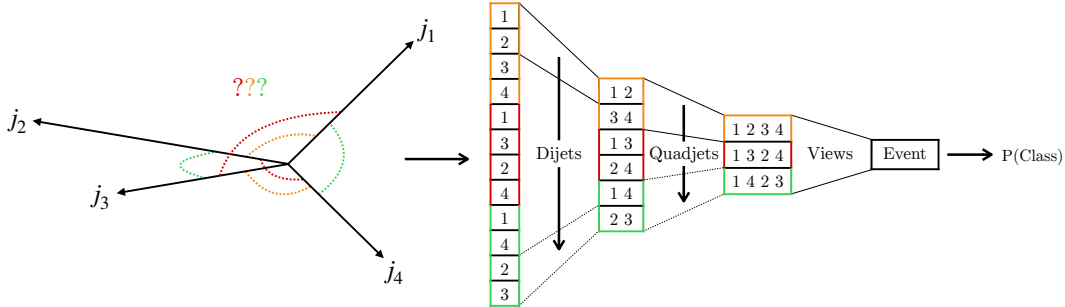


FIG 4. Illustration of the FvT classifier architecture.

$\hat{\beta}_4^s$ is called the FvT estimator, and we refer to $\hat{\psi}$ as the FvT (Four vs. Three) classifier. A careful choice of this classifier can dramatically increase the quality of fit, and we now describe a new classifier architecture specifically tailored to collider events of the type considered in this work.

4.2. *A Classifier for Collider Events.* We aim to design a classifier $\hat{\psi}$ over \mathcal{G} , which

- (a) is invariant to the ordering of the constituent jets in an input event g ;
- (b) is invariant with respect to the equivalence relation \simeq defined in (2.2);
- (c) incorporates the dijet substructure of an event $g = g^1 + g^2$.

We opt for a convolutional neural network architecture with residual layers, or ResNet (He et al., 2016), as depicted in Figure 4. An input event $g = \sum_{j=1}^4 p_{T_j} \delta_{(\eta_j, \phi_j, m_j)}$ to the network is treated as a one-dimensional image with 4 pixels, in any order, where each pixel corresponds to one jet parametrized by its coordinates $(p_{T_j}, \eta_j, \phi_j, m_j)$. The layers of the network are then designed as follows.

- (1) The 4 input pixels are duplicated twice to obtain an image with 12 pixels, such that all 6 possible pairs of dijets appear exactly once, consecutively in the image. Each such pair is then convolved into a one-dimensional image of six dijet pixels.
- (2) Each pair of dijets from this image is further convolved into an image with three pixels, consisting of the three possible pairing representations of the original four-jet, or quadjet, event.
- (3) The three quadjet pixels are combined into the last pixel representing the whole event.
- (4) A final output layer passes the event through a softmax activation function to produce the fitted probability $\hat{\psi}(g)$.

Notice that (c) is satisfied by construction of the network. We approximately impose (a) by replacing dijet pixels in step (2) by their sums and absolute values of their differences. Similar modifications may be made in (1) to render the network entirely invariant to relabelling of the input jets, as in (a), but we have observed increased performance by allowing the convolutions in step (1) to have information about the p_T ordering of the jets. Quadjet pixels from (2) are added together weighted by a real-valued score in step (3) to guarantee permutation invariance of the three pixels.

To enforce (b), recall that the network should be invariant under transformations $F_1^- : \eta \mapsto -\eta$, $F_2^- : \phi \mapsto -\phi$ and $F_2^\Delta : \phi \mapsto \phi + \Delta$, for any $\Delta \in [0, 2\pi)$, simultaneously across all constituent jets of an event. We enforce invariance under the former two transformations after step (3) by averaging the event-level pixel with its image under F_1^-, F_2^- . In principle, the same may be done to enforce invariance under the rotation F^Δ by averaging over a large

grid of candidate values Δ . To reduce the computational burden which would arise from such an operation, we instead apply random rotations Δ at each batch used in the Adam optimizer (Kingma and Ba, 2015) which we choose for training the network.

In steps (1)-(3), we also add engineered features specifically designed for dijet, quadjet, and event-level pixels respectively. These engineered features are designed such that they preserve invariance properties (a) and (b). For instance, in step (1) we insert pixels containing dijet masses and the Euclidean distance between dijet angular variables η_i, ϕ_i .

5. Background Modeling via Optimal Transport. The methodology described in the previous section hinged upon the ability of the classifier $\hat{\psi}$ to accurately extrapolate from the Control Region to the Signal Region, implying that the $3b$ and $4b$ intensity functions vary smoothly across these two regions. The validity of this assumption is difficult to verify in practice, and motivates us to develop a distinct approach with a complementary modeling assumption. In this section, rather than extrapolating the discrepancy between the $3b$ and $4b$ intensity functions, we will extrapolate the discrepancy between the intensity functions in the Control and Signal Regions, as illustrated in Figure 3.

We cannot use a density ratio to quantify the discrepancy between intensity functions in the Control and Signal Regions, because these regions are disjoint. We will instead use the notion of a *transport map*, which will be defined in the sequel. In order to employ transport maps, it will be convenient to normalize all intensity functions throughout this section. That is, we will define an estimator for β_4^s by separately estimating the probability measure $P_4^s = \beta_4^s / \beta_4^s(\mathcal{G}_s)$ and the normalization $\beta_4^s(\mathcal{G}_s)$. More generally, we write

$$P_j^c = \beta_j^c / \beta_j^c(\mathcal{G}_c), \quad P_j^s = \beta_j^s / \beta_j^s(\mathcal{G}_s), \quad j = 3, 4,$$

to denote the four population-level probability measures, with corresponding empirical measures

$$P_{3,n_a}^a = \frac{1}{n_a} \sum_{i=1}^{n_a} \delta_{H_i^a}, \quad P_{4,m_a}^a = \frac{1}{m_a} \sum_{i=1}^{m_a} \delta_{G_i^a}, \quad a \in \{c, s\}.$$

A transport map between P_3^c and P_3^s is any Borel-measurable function $T : \mathcal{G}_c \rightarrow \mathcal{G}_s$ such that whenever $H \sim P_3^c$, we have $T(H) \sim P_3^s$. When this condition holds, we write $P_3^s = T_{\#}P_3^c$, and we say T *pushes* P_3^c *forward* onto P_3^s , or that P_3^s is the *pushforward* of P_3^c under T . Equivalently, this condition holds if and only if

$$P_3^s(B) = T_{\#}P_3^c(B) = P_3^c(T^{-1}(B)), \quad \text{for all } B \in \mathbb{B}(\mathcal{G}_s).$$

We propose to perform background estimation under the following informal modeling assumption, which will be stated formally in the sequel.

ASSUMPTION 2'. *There exists a map $T_0 : \mathcal{G}_c \rightarrow \mathcal{G}_s$ such that*

$$(5.1) \quad T_{0\#}P_3^c = P_3^s, \quad \text{and} \quad T_{0\#}P_4^c = P_4^s.$$

Assumption 2' requires the $3b$ and $4b$ distributions to be sufficiently similar for there to exist a shared map T_0 which pushes forward their restrictions to the Control Region into their counterparts in the Signal Region. If such a map T_0 were available, it would suggest the following procedure for estimating P_4^s ,

- (a) Fit an estimator \hat{T} of T_0 based only on the $3b$ observations;
- (b) Given any estimator \hat{P}_{4,m_c}^c of P_4^c , use the pushforward $\hat{T}_{\#}\hat{P}_{4,m_c}^c$ as an estimator of P_4^s .

For this approach to be practical, we must specify an explicit candidate T_0 satisfying Assumption 2'. We propose to choose T_0 such that its movement of the probability mass from P_3^c into that of P_3^s is minimal. This leads us to consider the classical optimal transport problem, which we now describe.

5.1. *The Optimal Transport Problem.* Assume a metric W on the space \mathcal{G} is given; we provide a candidate for such a metric in Section 5.3. For any transport map T pushing P_3^c forward onto P_3^s , we refer to $W(h, T(h))$ as the cost of moving an event $h \in \mathcal{G}_c$ to an event $T(h) \in \mathcal{G}_s$. The optimal transport problem seeks to find the choice of T which minimizes the expected cost of transporting P_3^c onto P_3^s , which amounts to solving the following optimization problem

$$(5.2) \quad \operatorname{argmin}_{T: \mathcal{G}_c \rightarrow \mathcal{G}_s} \int_{\mathcal{G}_c} W(h, T(h)) dP_3^c(h), \quad \text{s.t. } T_{\#} P_3^c = P_3^s.$$

Equation (5.2) is known as the Monge problem (Monge, 1781). When a solution T_0 to the Monge problem exists, it is said to be an *optimal transport map*. We postulate that, when it exists, the optimal transport map from P_3^c to P_3^s is a sensible candidate for the map T_0 appearing in the statement of Assumption 2'.

A shortcoming of this choice is the requirement that there exist a solution to the optimization problem (5.2). It is well-known that the Monge problem over Euclidean space admits a unique solution for absolutely continuous distributions, when the cost function is the squared Euclidean norm (Knott and Smith, 1984; Brenier, 1991). While sufficient conditions for the solvability of the Monge problem in more general spaces are given by Villani (2008, Chapter 9), we do not know whether they are satisfied by the metric space (\mathcal{G}, W) under consideration. Furthermore, the Monge problem may not even be feasible between distributions which are not absolutely continuous, which precludes the possibility of estimating T_0 using the optimal transport map between the empirical measures of P_3^c and P_3^s .

Motivated by these considerations, we introduce a classical relaxation of the Monge problem, known as the Kantorovich optimal transport problem (Kantorovich, 1942, 1948). Let $\Pi(P_3^c, P_3^s)$ denote the set of all joint Borel distributions π over $\mathcal{G}_c \times \mathcal{G}_s$ whose marginals are respectively P_3^c and P_3^s , in the sense that $P_3^c(\cdot) = \pi(\cdot \times \mathcal{G}_s)$ and $P_3^s(\cdot) = \pi(\mathcal{G}_c \times \cdot)$. We refer to such joint distributions as *couplings*. Consider the minimization problem

$$(5.3) \quad \mathcal{W}(P_3^c, P_3^s) = \inf_{\pi \in \Pi(P_3^c, P_3^s)} \int_{\mathcal{G}_c \times \mathcal{G}_s} W(g, h) d\pi(g, h).$$

When the infimum in (5.3) is achieved by a coupling π_0 , this last is known as an *optimal coupling*. When an optimal coupling is supported on a set of the form $\{(h, T_0(h)) : h \in \mathcal{G}_c\}$, for some map $T_0 : \mathcal{G}_c \rightarrow \mathcal{G}_s$, it can be seen that T_0 is in fact an optimal transport map between P_3^c and P_3^s . The Kantorovich problem (5.3) is therefore a relaxation of the Monge problem (5.2). Unlike the latter, however, the minimization problem (5.3) is always feasible since $\Pi(P_3^c, P_3^s)$ is non-empty; indeed, $\Pi(P_3^c, P_3^s)$ always contains the independence coupling between P_3^c and P_3^s . Moreover, the infimum in the Kantorovich problem is achieved as soon as the cost function W is lower semi-continuous, and the measures P_3^c and P_3^s satisfy a mild moment condition (Villani (2008), Theorem 4.1). We also note that the optimal objective value $\mathcal{W}(P_3^c, P_3^s)$ defines a metric between probability measures called the (first-order) Wasserstein distance (Villani, 2003), or Earth Mover's distance (Rubner, Tomasi and Guibas, 2000).

Using the Kantorovich relaxation, we now formalize Assumption 2' into the following condition, which we shall require throughout the remainder of this section.

ASSUMPTION 2. *Assume there exists an optimal coupling $\pi_0 \in \Pi(P_3^c, P_3^s)$ between P_3^c and P_3^s . Given a pair of random variables $(H^c, H^s) \sim \pi_0$, let $\pi_0(\cdot|h)$ denote the conditional distribution of H^s given $H^c = h$, for any $h \in \mathcal{G}_c$. Then, the following implication holds:*

$$(5.4) \quad G^c \sim P_4^c \implies G^s | G^c \sim \pi_0(\cdot | G^c) \implies G^s \sim P_4^s.$$

Assumption 2 requires the $3b$ and $4b$ distributions to be sufficiently similar for their restrictions to the Signal and Control Regions to be related by a common conditional distribution. It further postulates that this conditional distribution is induced by the optimal coupling π_0 . Heuristically, $\pi_0(\cdot|H)$ plays the role of a multivalued optimal transport map for pushing an observation H from the distribution P_3^c onto P_3^s . Assumption 2 requires this map to additionally push the distribution P_4^c onto its counterpart P_4^s in the Signal Region. In the special case where there exists an optimal transport map T_0 from P_3^c to P_3^s , we note that $\pi_0 = (Id, T_0)_\# P_3^c$ is an optimal coupling of P_3^c with P_3^s , where Id denotes the identity map. In this case, equation (5.4) is tantamount to equation (5.1).

5.2. Background Estimation. We next derive estimators for the background distribution P_4^s under Assumption 2. Under this condition, it follows from equation (5.4) and the law of total probability that

$$P_4^s(\cdot) = \int_{\mathcal{G}^c} \pi_0(\cdot|g) dP_4^c(g).$$

Since $\pi_0(\cdot|g)$ is the distribution of H^s given $H^c = g$, it is an identified parameter which can be estimated using only the $3b$ data. Given an estimator $\hat{\pi}(\cdot|g)$ of this quantity, and an estimator \hat{P}_{4,m_c}^c of P_4^c , it is natural to consider the plugin estimator of the background distribution P_4^s , given by

$$(5.5) \quad \hat{P}_4^s(\cdot) := \int_{\mathcal{G}^c} \hat{\pi}(\cdot|g) d\hat{P}_{4,m_c}^c(g).$$

In what follows, we begin by defining an estimator $\hat{\pi}(\cdot|g)$ in Section 5.2.1, followed by two candidates for the estimator \hat{P}_{4,m_c} , leading to two distinct background estimation methods defined in Sections 5.2.2 and 5.2.3. In Section 5.2.4, we briefly discuss how these constructions also lead to estimators of the unnormalized intensity measure β_4^s . We then provide discussion and comparison of these methodologies in Section 5.2.5.

5.2.1. The Empirical Optimal Transport Coupling. A natural plugin estimator for the coupling π_0 is the optimal coupling $\hat{\pi}$ between the empirical measures P_{3,n_c}^c and P_{3,n_s}^s . In detail, denoting by $\hat{q} \in \mathbb{R}^{n_c \times n_s}$ the joint probability mass function of $\hat{\pi}$, the empirical Kantorovich problem takes the following form:

$$(5.6) \quad \hat{q} = (\hat{q}_{ij}) \in \underset{(q_{ij}) \subseteq \mathbb{R}^{n_c \times n_s}}{\operatorname{argmin}} \sum_{i=1}^{n_c} \sum_{j=1}^{n_s} q_{ij} W(H_i^c, H_j^s), \quad \text{s.t. } q_{ij} \geq 0, \quad \sum_{i=1}^{n_c} q_{ij} = \frac{1}{n_s}, \quad \sum_{j=1}^{n_s} q_{ij} = \frac{1}{n_c}.$$

Equation (5.6) is a finite-dimensional linear program, for which exact solutions may be computed using network simplex algorithms such as the Hungarian algorithm (Kuhn, 1955). We refer to Peyré and Cuturi (2019) for a survey. We then define the estimator $\hat{\pi}(\cdot|H_i^c)$, for $i = 1, \dots, n_c$, as the discrete distribution supported on $\{H_1^s, \dots, H_{n_s}^s\}$, with probability mass function defined by

$$\hat{q}_{j|i} = \frac{\hat{q}_{ij}}{\sum_{k=1}^{n_s} \hat{q}_{ik}} = n_c \cdot \hat{q}_{ij}, \quad j = 1, \dots, n_s.$$

With this definition in place, we are in a position to define estimators of the background distribution P_4^s .

5.2.2. *The OT- k NN Estimator.* We first consider the general estimator in equation (5.5) when \widehat{P}_{4,m_c}^c is the empirical measure P_{4,m_c}^c . This choice is perhaps most natural, but it requires us to perform out-of-sample evaluations of the estimator $\widehat{\pi}(\cdot|g)$. Indeed, recall that we merely defined the latter for all $g \in \{H_1^c, \dots, H_{n_c}^c\}$, whereas P_{4,m_c}^c is supported on the distinct set $\{G_1^c, \dots, G_{m_c}^c\}$.

We extend the support of $\widehat{\pi}(\cdot|g)$ to all $g \in \mathcal{G}$ using a variant of the method of nearest neighbors for nonparametric regression (Biau and Devroye, 2015). Let $k \geq 1$ be an integer. For all $g \in \mathcal{G}$, let $I_k(g)$ denote the indices of the k -nearest neighbors of g with respect to W , among $H_1^c, \dots, H_{n_c}^c$. Specifically, we set $I(g) = \{j_1, \dots, j_k\} \subseteq [n_c]$ where

$$W(g, H_{j_1}^c) \leq \dots \leq W(g, H_{j_k}^c) \leq W(g, H_j^c), \quad \text{for all } j \in [n_c] \setminus \{j_1, \dots, j_k\}.$$

Furthermore, define the inverse distance weights

$$(5.7) \quad \omega_i(g) = \frac{1/W(g, H_i^c)}{\sum_{l \in I_k(g)} 1/W(g, H_l^c)}, \quad i \in I_k(g),$$

with the convention $\infty/\infty = 1$. We then define for all $g \in \mathcal{G}$,

$$(5.8) \quad \widehat{\pi}_{\text{NN}}(\cdot|g) = \sum_{i \in I_k(g)} \omega_i(g) \widehat{\pi}(\cdot|H_i^c).$$

The estimator $\widehat{\pi}_{\text{NN}}(\cdot|g)$ couples g with all of the events to which its k -nearest neighbors are coupled under $\widehat{\pi}$. The coupling values which correspond to the closest nearest neighbors are assigned higher weights $\omega_i(g)$. Furthermore, we note that when $g \in \{H_1^c, \dots, H_{n_c}^c\}$, it holds that $\widehat{\pi}_{\text{NN}}(\cdot|g) = \widehat{\pi}(\cdot|g)$.

Using these definitions, the generic estimator in equation (5.5) takes the following form,

$$\widehat{P}_{4,\text{NN}}^s(\cdot) = \int \widehat{\pi}_{\text{NN}}(\cdot|g) dP_{4,m_c}^c(g) = \frac{1}{m_c} \sum_{\ell=1}^{m_c} \sum_{i \in I_k(G_\ell^c)} \omega_i(G_\ell^c) \widehat{\pi}(\cdot|H_i^c).$$

or equivalently,

$$\widehat{P}_{4,\text{NN}}^s = \frac{n_c}{m_c} \sum_{j=1}^{n_s} \left(\sum_{\ell=1}^{m_c} \sum_{i \in I_k(G_\ell^c)} \omega_i(G_\ell^c) \widehat{q}_{ij} \right) \delta_{H_j^s}.$$

We refer to $\widehat{P}_{4,\text{NN}}^s$ as the OT- k NN (Optimal Transport- k Nearest Neighbor) estimator of P_4^s .

5.2.3. *The OT-FvT Estimator.* It is known that the rate of production of $3b$ events typically exceeds that of $4b$ events by one order of magnitude (cf. Section 6). As a result, in the general formulation (5.5) of our optimal transport map estimators, we expect to have access to a smaller sample size m_c for estimating the distribution P_4^c , than the sample sizes n_c and n_s for estimating the optimal transport coupling π_0 . Motivated by this observation, we next define an estimator \widehat{P}_{4,m_c}^c which can leverage the larger $3b$ sample size n_c .

Let $p_j^c = dP_j^c/d\nu_0$ denote the density of P_j^c for $j = 3, 4$. Recall from Section 4 that for any event g , $\psi(g)$ denotes the probability that a random event G arose from the $4b$ distribution as opposed to the $3b$ distribution, given that $G = g$. Furthermore, $\widehat{\psi}(g)$ denotes the $[0, 1]$ -valued output of the FvT classifier for discriminating $4b$ events from $3b$ events. Recall further that for any $g \in \mathcal{G}_c$, it holds that $p_4^c(g)/p_3^c(g) = (\beta_3^c(\mathcal{G}_c)/\beta_4^c(\mathcal{G}_c)) \cdot (\psi(g)/(1 - \psi(g)))$, or equivalently,

$$P_4^c(B) = \frac{\beta_3^c(\mathcal{G}_c)}{\beta_4^c(\mathcal{G}_c)} \int_B \frac{\psi(h)}{1 - \psi(h)} dP_3^c(h), \quad B \in \mathbb{B}(\mathcal{G}_c).$$

We define a plugin estimator of the above quantity via

$$(5.9) \quad \widehat{P}_{4,m_c}^c(B) = \frac{n_c}{m_c} \int_B \frac{\widehat{\psi}(h)}{1 - \widehat{\psi}(h)} d\widehat{P}_{3,n_c}^c(h), \quad B \in \mathbb{B}(\mathcal{G}_c).$$

\widehat{P}_{4,m_c}^c can be viewed as a reweighted version of the empirical measure P_{3,n_c}^c . The weights are chosen to make the $3b$ sample resemble a $4b$ sample, by using the FvT classifier to estimate the density ratio p_4^c/p_3^c . Since the $3b$ sample is one order of magnitude larger than the $4b$ sample, we heuristically expect this estimator to have smaller theoretical risk than the empirical measure P_{4,m_c}^c whenever the density ratio p_4^c/p_3^c is smooth.

A second motivation for using the estimator \widehat{P}_{4,m_c}^c is the fact that it is supported on the domain of definition of the in-sample empirical optimal transport coupling $\widehat{\pi}(\cdot|g)$. We therefore do not need to extend the domain of this estimator, unlike the previous section. With these choices, the generic estimator in equation (5.5) takes the following form:

$$\widehat{P}_{4,\text{OF}}^s(\cdot) := \int_{\mathcal{G}_c} \widehat{\pi}(\cdot|g) d\widehat{P}_{4,m_c}^c(g) = \frac{1}{m_c} \sum_{i=1}^{n_c} \frac{\widehat{\psi}(H_i^c)}{1 - \widehat{\psi}(H_i^c)} \widehat{\pi}(\cdot|H_i^c),$$

or equivalently,

$$(5.10) \quad \widehat{P}_{4,\text{OF}}^s = \frac{n_c}{m_c} \sum_{j=1}^{n_s} \left(\sum_{i=1}^{n_c} \frac{\widehat{\psi}(H_i^c)}{1 - \widehat{\psi}(H_i^c)} \widehat{q}_{ij} \right) \delta_{H_j^s}.$$

We refer to $\widehat{P}_{4,\text{OF}}^s$ as the OT-FvT (Optimal Transport–Four vs. Three) estimator of P_4^s .

5.2.4. Estimation of the Background Normalization. For completeness, we briefly explain how the OT- k NN and OT-FvT estimators can also be used to estimate the unnormalized background intensity function β_4^s . We employ the widely-used ABCD method (Alison, 2015; Aad et al., 2015; Choi and Oh, 2021; Kasieczka et al., 2021), which requires the following assumption.

ASSUMPTION 3. *It holds that $\beta_4^s(\mathcal{G}_s) = \beta_3^s(\mathcal{G}_s) \frac{\beta_4^c(\mathcal{G}_c)}{\beta_3^c(\mathcal{G}_c)}$.*

Assumption 3 implies that the ratio of the number of $4b$ to $3b$ events in the Control Region should be roughly proportional to that in the Signal Region. Under this assumption, a natural estimator for $\beta_4^s(\mathcal{G}_s)$ is simply given by $m_c n_s / n_c$. Therefore, under Assumptions 2–3, the probability measures $\widehat{P}_{4,\text{NN}}^s$ and $\widehat{P}_{4,\text{OF}}^s$ can be used to define the following two estimators of the unnormalized background intensity measure β_4^s ,

$$(5.11) \quad \widehat{\beta}_{4,\text{NN}}^s = \frac{m_c n_s}{n_c} P_{4,\text{NN}}^s, \quad \widehat{\beta}_{4,\text{OF}}^s = \frac{m_c n_s}{n_c} P_{4,\text{OF}}^s.$$

We respectively refer to the above measures as the OT- k NN and OT-FvT estimators of β_4^s , or simply as the OT- k NN and OT-FvT methods.

5.2.5. Remarks. We summarize the three background estimation methods FvT, OT- k NN and OT-FvT, in Table 1, and we make the following remarks.

- Assumption 2 is the primary modeling assumption required by OT- k NN and OT-FvT. We view this condition as being complementary to Assumption 1(ii), required by the FvT method. Indeed, it involves an extrapolation (of an optimal coupling) from the $3b$ to $4b$ distributions, rather than an extrapolation (of a density ratio) from the Control Region to the Signal Region.

TABLE 1

Summary of the three background estimation methods: FvT, OT-kNN, and OT-FvT. The final estimator for each method takes the form $\hat{\beta}_4^s \propto \sum_{j=1}^{n_s} v_j \delta_{H_j^s}$, for the values of v_j listed in the table.

Estimator (of the form $\propto \sum_{j=1}^{n_s} v_j \delta_{H_j^s}$)	FvT	OT-FvT	OT-kNN
v_j	$\frac{\hat{\psi}(H_i^s)}{1 - \hat{\psi}(H_i^s)}$	$\sum_{i=1}^{n_c} \frac{\hat{\psi}(H_i^c)}{1 - \hat{\psi}(H_i^c)} \hat{q}_{ij}$	$\sum_{\ell=1}^{m_c} \sum_{i \in I_k(G_\ell^c)} \omega_i(G_\ell^c) \hat{q}_{ij}$

- The OT-FvT estimator (5.10) can alternatively be interpreted through the lens of domain adaptation for the FvT classifier. To make this connection clear, suppose for simplicity that $n_c = m_c$. In this case, it can be shown that $\hat{\pi}$ is in fact induced by an optimal transport map, in the sense that there exists a permutation $\hat{\tau} : [n_c] \rightarrow [n_c]$ such that

$$\hat{q}_{ij} = I(i = \hat{\tau}(j)) / n_c, \quad i, j = 1, \dots, n_c.$$

The FvT and OT-FvT estimators then take the following form:

$$\hat{\beta}_{4,\text{FvT}}^s \propto \sum_{j=1}^{n_s} \frac{\hat{\psi}(H_j^s)}{1 - \hat{\psi}(H_j^s)} \delta_{H_j^s}, \quad \hat{\beta}_{4,\text{OF}}^s \propto \sum_{j=1}^{n_s} \frac{\hat{\psi}(H_{\hat{\tau}(j)}^c)}{1 - \hat{\psi}(H_{\hat{\tau}(j)}^c)} \delta_{H_j^s}.$$

While the FvT method evaluates the density ratio estimator $\hat{\psi}/(1 - \hat{\psi})$ at events H_j^s in the Signal Region, the OT-FvT method evaluates it at the events $H_{\hat{\tau}(j)}^c$ in the Control Region, to which the events H_j^s are mapped under the empirical optimal coupling $\hat{\pi}$. The OT-FvT method thus circumvents the evaluation of $\hat{\psi}$ outside the region where it was fitted. Optimal transport has similarly been used in past literature as a tool for domain adaptation between train and test data in classification problems (cf. Section 1.2).

- In defining the estimator OT-kNN, we proposed to extend the domain of definition of the empirical optimal transport coupling $\hat{\pi}(\cdot|g)$ to the entire space \mathcal{G}_c via nearest neighbor extrapolation; cf. equation (5.8). It was shown by Manole et al. (2021) that, for the quadratic optimal transport problem over Euclidean space, such a procedure has statistically minimax optimal risk for estimating the underlying optimal transport map T_0 , assuming that it exists and is Lipschitz continuous. Nevertheless, the risk of this estimator suffers severely from the curse of dimensionality, and does not generally improve when T_0 enjoys higher regularity. Manole et al. (2021) and Deb, Ghosal and Sen (2021) have instead shown that plugin estimators of T_0 based on density estimates of P_3^c and P_3^s may achieve improved convergence rates in such settings. In our context, it is challenging to perform density estimation over the space of measures \mathcal{G} —and particularly over the non-convex set \mathcal{G}_c —thus we did not follow this approach. Our aim was instead to alleviate the curse of dimensionality inherent to the OT-kNN method by introducing the OT-FvT method. Indeed, we view the task of estimating P_4^c as a larger statistical bottleneck than that of estimating π_0 , and the estimator \hat{P}_{4,m_c}^c (used by the OT-FvT method) may potentially achieve smaller risk than the empirical measure P_{4,m_c}^c (used by the OT-kNN method).
- Manole et al. (2021) additionally show that the value $k = 1$ suffices for the estimator $\hat{\pi}_{\text{NN}}$ to enjoy optimal theoretical risk, at least for the quadratic optimal transport problem over Euclidean space. In our work, we nevertheless allow for k to be greater than 1 in order to leverage the larger size of the $3b$ sample. For example, when $k = 1$, the estimator $\hat{\beta}_{4,\text{NN}}^s$ is supported on at most m_c events, whereas it can be supported on as many as $n_s \gg m_c$ events if k is chosen sufficiently large. In practice, we recommend choosing k to be as small as possible while ensuring that $\hat{\beta}_{4,\text{NN}}^s$ has support size nearly equal to m_c —this

typically amounts to choosing k to be on the order of n_s/m_c . In our simulation study (cf. Section 6), we therefore choose the value $k = 10$, but also illustrate the performance of the OT- k NN method for other values of k .

- We have chosen to separately estimate the probability measure P_4^s and the normalization $\beta_4^s(\mathcal{G}_s)$, because the classical optimal transport problem is only well-defined between measures with the same total mass. A possible alternative is to consider the *partial* (Figalli, 2010) or *unbalanced* (Liero, Mielke and Savaré, 2018) optimal transport problems between the unnormalized intensity measures β_3^c and β_3^s . These variants of optimal transport are well-defined between measures that have possibly different mass, but have the downside of introducing tuning parameters. As we explain in Section 6, the normalizations $\beta_3^c(\mathcal{G}_c)$ and $\beta_3^s(\mathcal{G}_s)$ are of the same order of magnitude, thus we have simply focused our attention on the classical (balanced) optimal transport problem in this work. Nevertheless, in the following subsection, we will employ a variant of the partial optimal transport problem to define the metric W .

5.3. A Metric between Collider Events. We now describe a candidate for the metric W on \mathcal{G} . Recall that the Kantorovich problem in (5.3) gave rise to the Wasserstein distance \mathcal{W} between probability distributions over \mathcal{G} . By a recursion of ideas, we will also define W to be a Wasserstein-type metric, arising from the optimal transport problem between constituent jets of events. Such an approach was first proposed by Komiske, Metodiev and Thaler (2019). They propose to metrize \mathcal{G} using a variant of the Wasserstein distance which is well-defined between measures with non-equal mass (Peleg, Werman and Rom, 1989; Pele and Werman, 2008). Given any two collider events $g = \sum_{j=1}^4 p_{T_j} \delta_{(\eta_j, \phi_j, m_j)}$, $h = \sum_{j=1}^4 p'_{T_j} \delta_{(\eta'_j, \phi'_j, m'_j)} \in \mathcal{G}$, the metric is defined by

$$(5.12) \quad \begin{aligned} \widetilde{W}(g, h) = & \min_{(f_{ij}) \in \mathbb{R}^{4 \times 4}} \frac{1}{R} \sum_{i=1}^4 \sum_{j=1}^4 f_{ij} \sqrt{(\eta_i - \eta'_j)^2 + (\phi_i - \phi'_j)^2} + \left| \sum_{i=1}^4 (p_{T_i} - p'_{T_i}) \right| \\ \text{s.t. } & f_{ij} \geq 0, \quad \sum_j f_{ij} \leq p_{T_i}, \quad \sum_i f_{ij} \leq p'_{T_j}, \quad \sum_{i,j} f_{ij} = \min\left(\sum_i p_{T_i}, \sum_j p'_{T_j}\right), \end{aligned}$$

for a tuning parameter $R > 0$. We make several remarks about this definition.

- In the context of particle physics, the coupling f_{ij} is naturally interpreted as a flow of energy (measured in terms of the transverse momentum p_T) from jet i of g to jet j of h , as depicted in Figure 5. $\widetilde{W}(g, h)$ thus measures the smallest possible transport of energy required to rearrange the jets of the event g into those of h .
- We have followed Komiske, Metodiev and Thaler (2019) by omitting the mass variables m_j and m'_j from the definition of \widetilde{W} . This choice is further discussed in the context of our simulation study in Section 6.
- The tuning parameter R induces a trade-off between the influence of the angular variables ϕ_i, η_i , and that of the energy variables p_{T_i} . Our choice of R is further discussed in Section 6.

The metric \widetilde{W} does not, however, take into account the equivalence relation \simeq over \mathcal{G} defined in equation (2.2). For example, $\widetilde{W}(g, h)$ could be nonzero even when g and h are deemed equivalent for our purposes. We therefore define our final metric W by

$$(5.13) \quad W(g, h) = \inf \left\{ \widetilde{W}(g', h) : g' \simeq g, g' \in \mathcal{G} \right\}, \quad g, h \in \mathcal{G}.$$

Strictly speaking, W now becomes a metric over the set of equivalence classes of events induced by \simeq . We refer to Figure 5 for an illustration.

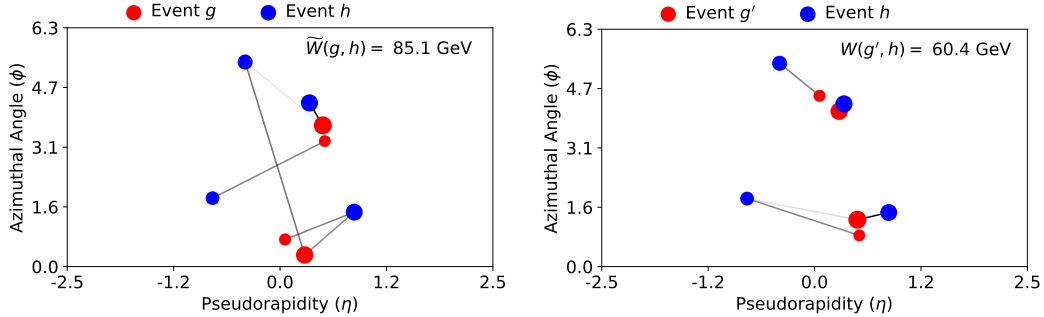


FIG 5. *Left:* (η, ϕ) -plot of two events $g, h \in \mathcal{G}$. Each point represents a constituent jet, with size proportional to its p_T value. A line connecting the i -th jet of event g to the j -th jet of event h indicates a nonzero value of the optimal coupling f_{ij} , with line darkness increasing as a function of the magnitude of f_{ij} . *Right:* (η, ϕ) -plot of events $g', h \in \mathcal{G}$, where $g' \simeq g$ is an approximate minimizer in equation (5.13). It can be seen that distance $W(g, h) = W(g', h) < \tilde{W}(g, h)$.

6. Simulation Study.

6.1. *Simulation Description.* In this section, we compare the performance of the three background modeling methods OT-FvT, OT- k NN and FvT, on realistic simulated collider data, generated using the MadGraph particle physics software (Alwall et al., 2011). Code for reproducing this simulation study is publicly available³.

Since b -tagging is imperfect, in practice, we expect the $3b$ and $4b$ samples to be composed of a mixture of different multijet scattering processes which do necessarily arise from b -quarks. We perform a study in MadGraph to estimate the relative scale of such processes. Assuming a b -jet tagging efficiency of 75%, a charm jet tagging efficiency of 15% and a light jet tagging efficiency of 1%, we find that the $4b$ (resp. $3b$) sample consists of 90% (10%) events in a final state with four b quarks, 7% (9%) events in a final state with two b quarks and two charm quarks, and 4% (80%) in a final state with two b quarks and two light quarks. In particular, we stress that a fraction of the $3b$ sample consists of mislabelled $4b$ events, which could be signal events. This signal contamination is expected to be sufficiently small to be considered negligible for purposes of a signal discovery analysis, as in this paper.

We generate four-quark events in MadGraph according to the percentages listed above. The calorimeters in the CMS detector are not perfect, and the measured jet energies have a finite resolution. The distribution of the observed smeared energy is well-approximated by the Gaussian distribution $N(E, \sigma^2(E))$, where E denotes the true energy of a jet, and $\sigma(E)$ satisfies

$$\left(\frac{\sigma(E)}{E}\right)^2 = \left(\frac{S}{\sqrt{E}}\right)^2 + \left(\frac{N}{E}\right)^2 + C^2,$$

for some fixed constants $S, N, C \geq 0$. We apply this smearing to the quark four-vectors, setting $S = 0.98, N = 0, C = 0.054$. For simplicity we set the quark masses to zero and omit them from the the metric W . When applying these methods to real data, it may, however, be useful to incorporate the jet masses into the definition of W . We also apply jet-level scale factors to account for the p_T dependence of CMS b -tagging for light, charm and bottom quark

³<https://github.com/tmanole/HH4bsim>

jets:

$$\text{Scale Factor} = \begin{cases} (2.5 p_T e^{-7 p_T} + 0.6)/0.75 & b\text{-quark} \\ (p_T e^{-10 p_T} + 0.2)/0.15 & c\text{-quark} \\ (0.03 p_T + 0.01)/0.01 & u, d, s\text{-quark or gluon,} \end{cases}$$

where p_T is measured in TeV. Events are weighted by the product of the scale factors for the b -tagged jets.

Following this pre-processing of the data, the pairing algorithm described in Section 3.2 is applied to all events, and those falling within the Control and Signal Regions are kept. We define these regions according to equations (3.7–3.8), with the parameters $\sigma_c = 1.03$, $\kappa_s = 1.6$ and $\kappa_c = 30$. The final sample consists of $n_s = 201,568$ events in the $3b$ Signal Region, $n_c = 159,427$ events in the $3b$ Control Region, $m_s = 28,980$ events in the $4b$ Signal Region, and $m_c = 22,053$ events in the $4b$ Control Region. The order of magnitude of these sample sizes, as well as the proportion of $3b$ to $4b$ events, is similar to those used in recent di-Higgs analyses at the LHC (ATLAS, 2019). We further simulate a separate $4b$ sample of size approximately $10(n_s + m_s)$, which we choose not to contain any signal events, and whose distribution we treat as the ground truth for the purpose of validating our background models.

We additionally generate a Monte Carlo sample from the SM di-Higgs signal distribution, with which the signal intensity rates $(S_j)_{j=1}^J$, used to form the likelihood function (3.5), can be specified. For the purpose of validating our background models, we train a $[0, 1]$ -valued classifier \hat{h} (abbr. Signal vs. Background, or SvB, classifier) to discriminate the $4b$ data from the Monte Carlo di-Higgs sample. Given that our simulated $4b$ sample contains no signal events, \hat{h} forms a reasonable proxy for the theoretical binning function h in equation (3.6). The SvB classifier has the same architecture as that of the FvT classifier described in Section 4.2. In the sequel, we refer to $\hat{h}(g)$ as the SvB value corresponding to an event g .

Finally, we discuss our choice of the parameter R arising in the definition of the metric W . In order for the two terms in the definition of \widetilde{W} to be of comparable order, we make the requirement that R lie within the range of the first summand in equation (5.12). We identify this range as follows. Since b -tagging is only performed for values of η lying in the interval $[-2.5, 2.5]$, we impose $R \leq \sqrt{\pi^2 + 5^2} \approx 5.9$. Furthermore, jet clustering algorithms used by CMS merge particles whose (η, ϕ) -Euclidean distance is within 0.4 (Cacciari, Salam and Soyez, 2008; CMS, 2017), thus we impose $R \geq 0.4$. Now, since we expect that the largest discrepancies between the Control and Signal Region distributions arise in the kinematic variables (η, ϕ) , we choose the smallest possible value $R = 0.4$ when fitting the empirical optimal transport coupling $\hat{\pi}$. On the other hand, for the nearest-neighbor lookup of the OT- k NN method, we set $R = 2.75$, which is the midpoint of the interval $[0.4, 5.9]$. We make no attempt to tune these values of R , and we leave open the question of choosing them in a data-driven fashion. We compute the metric W in part using the EnergyFlow Python library (Komiske, Metodiev and Thaler, 2022), and we compute optimal couplings between distributions of collider events using the Python Optimal Transport library (Flamary et al., 2021)

6.2. Simulation Results. The fitted intensity measures $\hat{\beta}_4^s$ produced by the three background methods (FvT, OT- k NN and OT-FvT) are binned and plotted in Figure 6. Logarithmic scales are used to better visualize signal-rich regions. Plots with additional kinematic variables are given in Appendix A. It can be seen that the three methods yield qualitatively similar estimates of the SvB intensity function. We recall that the SvB variable is of primary interest to model, as it is used as the final discriminant when testing the signal hypothesis (3.1). The m_{HH} variable has also been used as the final discriminant in recent di-Higgs studies (Bryant,

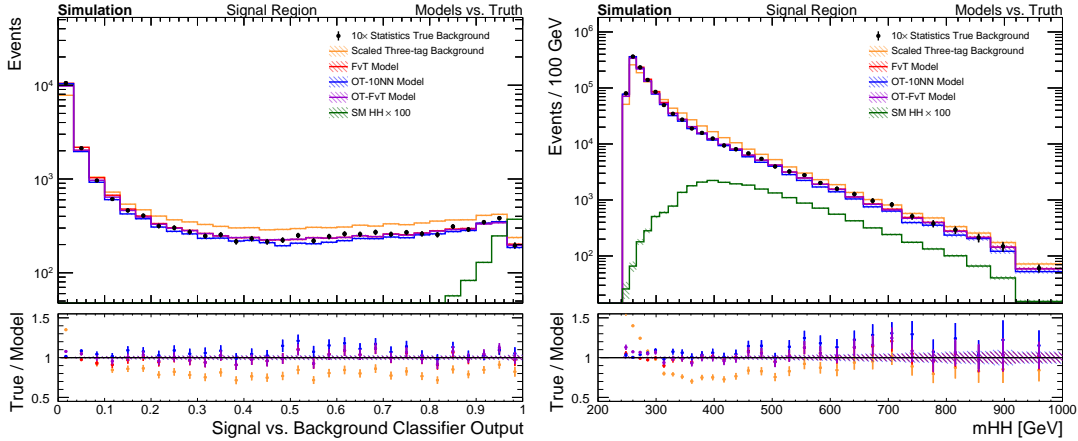


FIG 6. Histograms of the the SvB classifier output variable (left) and the m_{HH} variable (right) for the three background models as well as the upsampled $4b$ data (treated as the ground truth), the $3b$ data (normalized by the factor $n_{s\text{m}c}/n_c$), and the di-Higgs signal sample (SM HH). Error bars in the k -th bin of any histogram denote $\pm\sqrt{N_k}$, where N_k is the number of events per bin. Error bars in the ratio plot denote $\pm\sqrt{N_k}/N_{0k}$, where N_{0k} is the number of observed $4b$ events per bin. The dashed lines in the ratio plot denote $\pm\sqrt{1/N_{0k}}$.

2018). Given an event $g \in \mathcal{G}$ with dijet pairing $\{g^1, g^2\}$, its m_{HH} value is defined as follows⁴, using the notation of Section 3.2,

$$(6.1) \quad m_{\text{HH}}(g) = m \left(\frac{m_{\text{H}}}{m(g^1)} g^1 + \frac{m_{\text{H}}}{m(g^2)} g^2 \right).$$

Once again, we observe that this variable is well-modelled by all three methods. Among the various kinematic variables which we analyzed, the “ ΔR_{jj} –Other” variable, appearing in Figure 12 of Appendix A, presents one of the largest qualitative discrepancies between the three methods, and appears to be best-modelled by the FvT method. In all cases, it can be seen that the three methods provide a significant improvement compared to the uncorrected $3b$ sample.

In order to provide a quantitative comparison of these methods, we develop a heuristic two-sample test for testing equality between the distribution of the fitted background models and of the true upsampled $4b$ data. Specifically, we form a proxy for a two-sample test by training classifiers to discriminate each of the background estimates from the upsampled $4b$ data. Intuitively, if a background estimate is accurate, then a classifier should not be able to tell it apart from the true data. For each classifier, we record the area under the receiver operating characteristic curve (AUC; Hanley and McNeil (1982)), and any deviation of this quantity from .5 is an indication of mismodeling. We again choose our classifiers to be residual neural networks with the architecture described in Section 4.2. Although this choice is inherently favourable to the FvT method, and to some extent the OT-FvT method, we use it because it also coincides with the SvB classifier architecture, and will thus be most powerful at detecting mismodeling in the features which are relevant for the final signal analysis.

⁴Equation (6.1) can be interpreted as the four-body invariant mass after the dijet four-vectors have been corrected to have the Higgs boson mass.

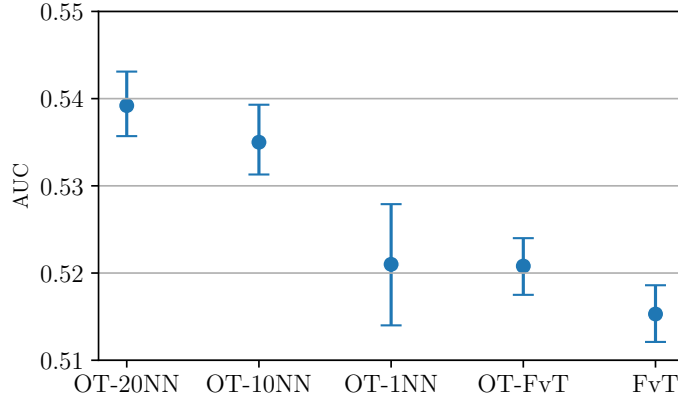


FIG 7. Fitted AUC values obtained by discriminating each background model from the upsampled 4b data using the FvT classifier; together with 95% percentile bootstrap variability intervals, obtained by bootstrapping the predicted classifier probabilities. 1,000 bootstrap replications are used. Note that this bootstrap procedure does not take into account the variability of the background estimators themselves. For the 3b-tagged data, we obtain the AUC 0.5843, with variability interval [0.5812, 0.5874].

The fitted AUC value for each method is reported in Figure 7. Though all AUCs are significantly greater than .5, they are substantially lower for our background models than for the benchmark method consisting of the uncorrected 3b sample. The FvT method has the lowest AUC, followed by the OT-FvT method and OT- k NN method. While the OT-1NN method has comparable AUC point estimate as the OT-FvT method, we emphasize that its variability interval is wider, which could have been anticipated from the discussion in Section 5.2.5. The performance of the OT- k NN method for varying values of k , along the SvB and m_{HH} variables, is illustrated in Figure 9.

We next provide a qualitative comparison of the fitted weights produced by the three background modeling methods. Recall that these methods all take the form

$$\hat{\beta}_4^s = \sum_{i=1}^{n_s} v_i \delta_{H_i^s},$$

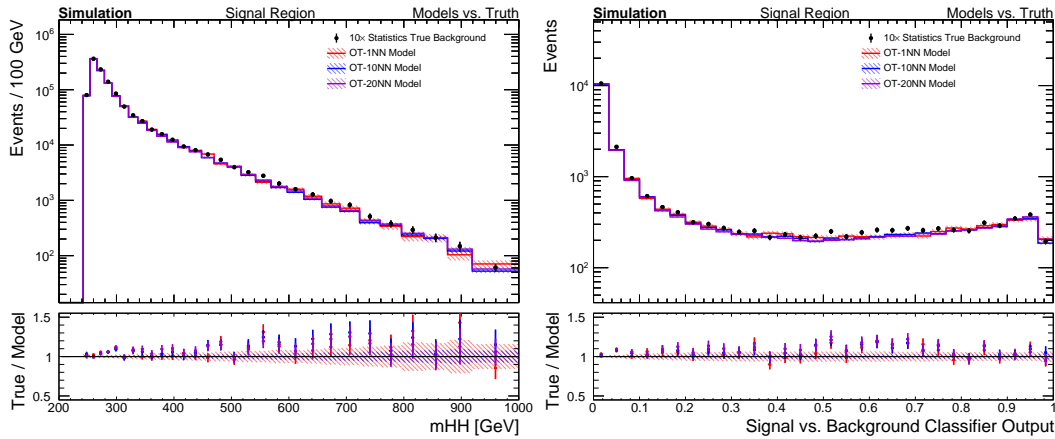


FIG 8. Histograms of the SvB classifier output variable (left) and the m_{HH} variable (right) for the OT- k NN estimator, with $k \in \{1, 10, 20\}$.

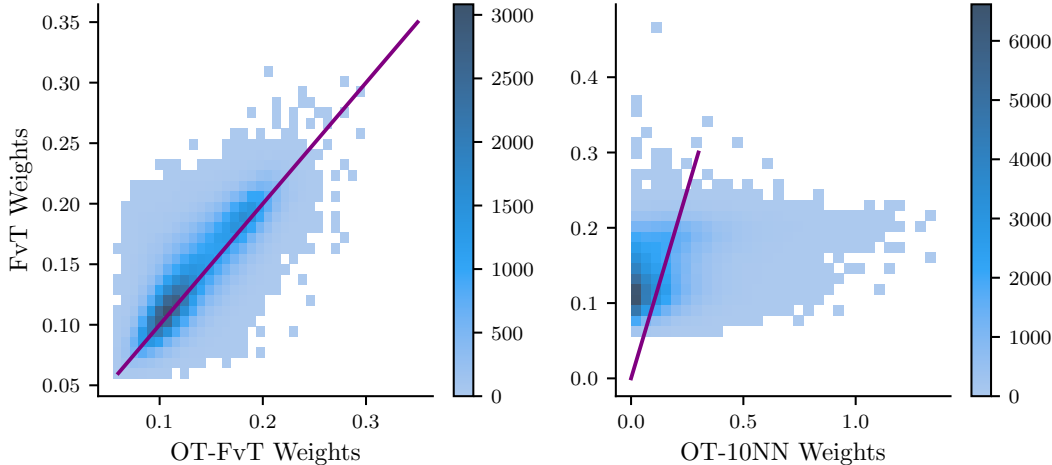


FIG 9. Bivariate histogram of the $3b$ data $H_1^s, \dots, H_{n_s}^s$ in the Signal Region, plotted in terms of the weights of the OT-FvT method against those of the FvT method (left), and of the OT-10NN method against those of the FvT method (right). The purple lines denote the identity function.

for some nonnegative weights v_i , which are summarized up to normalization in Table 1. In Figure 9, we plot the weights of the two optimal transport methods against those of the FvT method. We observe that the FvT and OT-FvT methods produce weights which are concentrated and symmetric around the identity. This implies that the odds ratio of the FvT classifier at a point H_j^s in the Signal Region behaves similarly to the odds ratio at any point H_i^c in the Control Region to which H_j^s is optimally coupled. This suggests that the transfer learning of the FvT classifier from the Control Region to the Signal Region is, to some extent, well-modelled by the optimal transport coupling $\hat{\pi}$. This observation heuristically suggests that Assumptions 1–2 both hold in this simulation. In contrast to the method OT-FvT, we observe that the method OT-10NN produces markedly different weights than the FvT method, which can partly be anticipated from the discrete nature of the nearest neighbor extrapolation. We conjecture that the nearest-neighbor estimator of the optimal transport coupling has poorer theoretical risk than its counterpart in the OT-FvT method.

7. Conclusion and Discussion. Our aim has been to study the problem of data-driven background estimation, motivated by the ongoing search for double Higgs boson production in the $4b$ final state. After recalling a widely-used approach to this problem based on transfer learning of a multivariate classifier, our first contribution was to develop the FvT classifier architecture which is tailored to collider data, and which can serve as a powerful tool for implementing this methodology. Our second contribution has been to propose a distinct background estimation method based on the optimal transport problem. A recurring theme throughout our work has been the complementarity of the modeling assumptions made by these two distinct approaches, which allows them to be used as cross-checks for one another in practice. We substantiate this point with a realistic simulation study, in which these methodologies appear to give consistent results despite their inherently distinct derivations.

Quantifying the uncertainty of our background estimates is a challenging problem left open by our work, which is nonetheless crucial for applying our methods in practice. In the experimental particle physics community, it is commonplace to measure both *statistical* uncertainties—those arising from fluctuations of the data generating process—and *systematic* uncertainties—those arising from potential mismodeling (Heinrich and Lyons, 2007). Both of these forms of uncertainty are challenging to quantify in our context. For instance, a

prerequisite for quantifying the statistical uncertainty of the methods OT- k NN or OT-FvT is to perform statistical inference for optimal transport maps. This is a difficult open problem in the statistical optimal transport literature, that has only been addressed for some special cases (Rippl, Munk and Sturm, 2016; Ramdas, Trillos and Cuturi, 2017), and for regularized variants of optimal transport maps which differ from those used in our work (Klatt, Taming and Munk, 2020; Gunsilius and Xu, 2021; González-Sanz, Loubes and Niles-Weed, 2022; Goldfeld et al., 2022). The question of quantifying systematic uncertainties is more open-ended, and typically involves heuristics for assessing the extent of potential mismodeling by the background estimation methods. Due to the complementarity of assumptions placed by our methods, any lack of closure between them could potentially play a role in quantifying their systematic uncertainties. While further investigation is required to make such a proposal formal, it is our hope that the optimal transport methodology presented in our work can help contribute to the challenging question of systematic uncertainty quantification in the search for di-Higgs boson production, or in other searches at the Large Hadron Collider.

Acknowledgments. We are grateful to the CMU Statistical Methods for the Physical Sciences (STAMPS) research group for insightful discussions and feedback throughout this work.

Funding. This work was supported in part by NSF PHY-2020295 and NSF DMS-2053804. TM was supported in part by the Natural Sciences and Engineering Research Council of Canada (NSERC), through a PGS D scholarship.

APPENDIX A: ADDITIONAL SIMULATIONS RESULTS

In this appendix, we report additional results from the simulation study in Section 6.

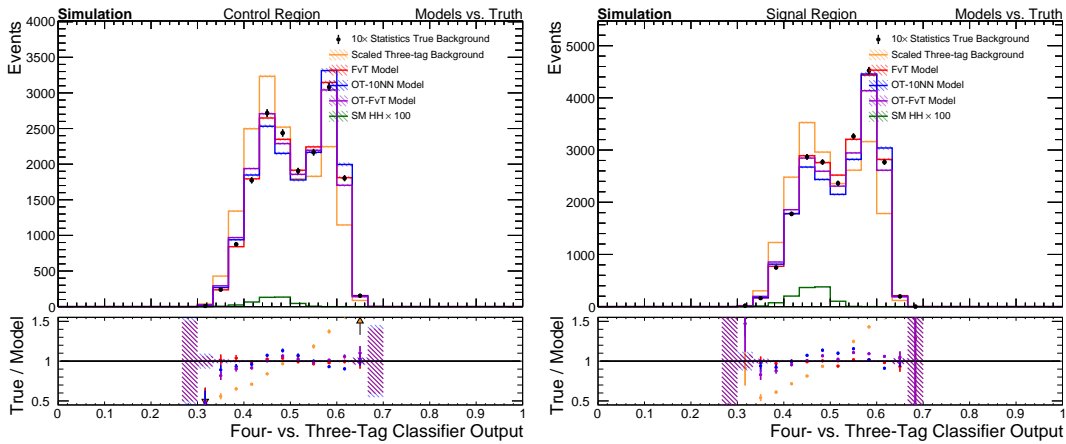


FIG 10. Histograms of the FvT classifier output variable in the Control Region (left) and the Signal Region (right), for the three background models as well as the upsampled 4b data (treated as the ground truth), the 3b data (normalized by the factor $n_s m_c / n_c$), and the di-Higgs signal sample (SM HH).

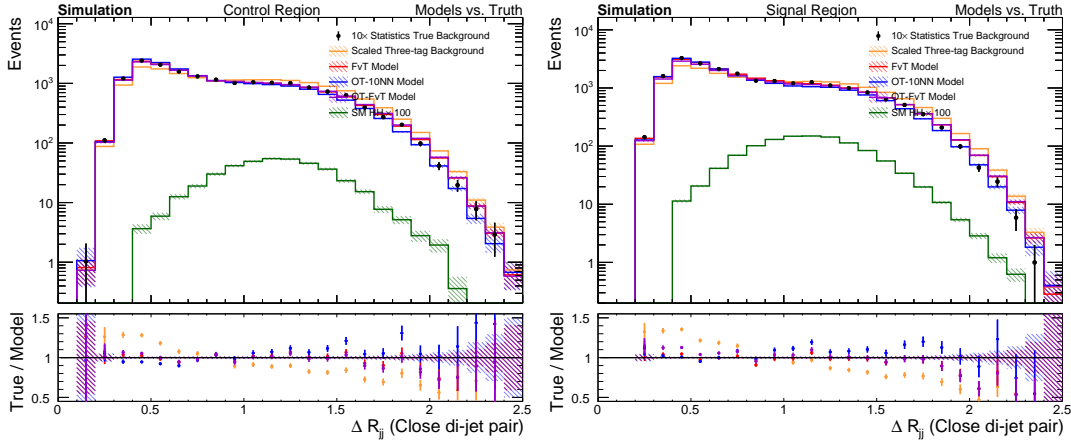


FIG 11. Histograms of the “ ΔR_{jj} –Close” variable (defined as the angular distance between the two closest jets of an event) in the Control Region (left) and the Signal Region (right), for the three background models as well as the upsampled $4b$ data (treated as the ground truth), the $3b$ data (normalized by the factor $n_s m_c / n_c$), and the di-Higgs signal sample (SM HH).

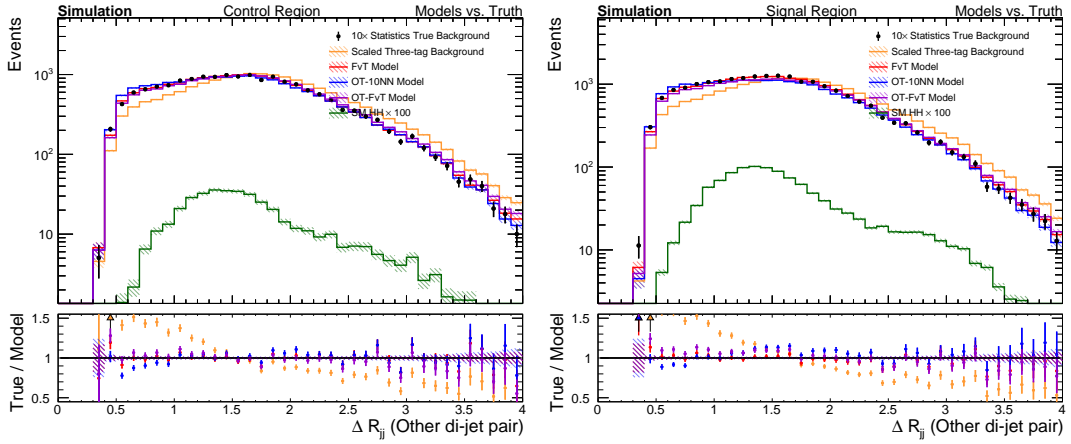


FIG 12. Histograms of the “ ΔR_{jj} –Other” variable (defined as the angular distance between the two jets of an event other than the two which are closest) in the Control Region (left) and the Signal Region (right), for the three background models as well as the upsampled $4b$ data (treated as the ground truth), the $3b$ data (normalized by the factor $n_s m_c / n_c$), and the di-Higgs signal sample (SM HH).

REFERENCES

- AAD, G. et al. (2015). Observation and measurement of Higgs boson decays to WW^* with the ATLAS detector. *Phys. Rev. D* **92** 012006.
- ALISON, J. (2015). The Road to Discovery: Detector Alignment, Electron Identification, Particle Misidentification, WW Physics, and the Discovery of the Higgs Boson, PhD thesis Presented 08 Nov 2012.
- ALLWALL, J., HERQUET, M., MALTONI, F., MATTELAER, O. and STELZER, T. (2011). MadGraph 5: going beyond. *Journal of High Energy Physics* **2011** 128.
- ATLAS Search for non-resonant pair production of Higgs bosons in the $\bar{b}b\bar{b}b$ final state in pp collisions at $\sqrt{s} = 13$ TeV with the ATLAS detector Technical Report, CERN, Geneva ATLAS-CONF-2022-035.

- ATLAS (2012). Observation of a new particle in the search for the Standard Model Higgs boson with the ATLAS detector at the LHC. *Physics Letters B* **716** 1–29.
- ATLAS (2018a). Search for pair production of higgsinos in final states with at least three b-tagged jets in $\sqrt{s} = 13$ TeV pp collisions using the ATLAS detector. *Physical Review D* **98**.
- ATLAS (2018b). Observation of $H \rightarrow bb$ decays and VH production with the ATLAS detector. *Physics Letters B* **786** 59–86.
- ATLAS (2018c). Measurements of Higgs boson properties in the diphoton decay channel with 36 fb⁻¹ of pp collision data at $\sqrt{s} = 13$ TeV with the ATLAS detector. *Physical review D* **98** 052005.
- ATLAS (2018d). Measurement of gluon fusion and vector-boson-fusion Higgs boson production cross-sections in the $H \rightarrow WW^* \rightarrow e\nu\mu\nu$ decay channel in pp collisions at $\sqrt{s} = 13$ TeV with the ATLAS detector. ATLAS-CONF-2018-004.
- ATLAS (2018e). Measurements of the Higgs boson production, fiducial and differential cross sections in the 4ℓ decay channel at $\sqrt{s} = 13$ TeV with the ATLAS detector. ATLAS-CONF-2018-018.
- ATLAS (2019). Search for pair production of Higgs bosons in the $b\bar{b}b\bar{b}$ final state using proton-proton collisions at $\sqrt{s} = 13$ TeV with the ATLAS detector. *Journal of High Energy Physics* **2019** 30.
- ATLAS (2021). Search for the $HH \rightarrow b\bar{b}b\bar{b}$ process via vector-boson fusion production using proton-proton collisions at $\sqrt{s} = 13$ TeV with the ATLAS detector. *Journal of High Energy Physics* **2021**.
- ATLAS, CMS and HIGGS COMBINATION GROUP (2011). Procedure for the LHC Higgs boson search combination in Summer 2011. CMS-NOTE-2011-005. ATL-PHYS-PUB-2011-11.
- BARLOW, R. (1987). Event Classification Using Weighting Methods. *Journal of Computational Physics* **72** 202–219.
- BEHNKE, O., KRÖNINGER, K., SCHOTT, G. and SCHÖRNER-SADENIUS, T. (2013). *Data Analysis in High Energy Physics: A Practical Guide to Statistical Methods*. John Wiley & Sons.
- BIAU, G. and DEVROYE, L. (2015). *Lectures on the nearest neighbor method*. Springer.
- BORISYAK, M. and KAZEEV, N. (2019). Machine Learning on Data with sPlot Background Subtraction. *Journal of Instrumentation* **14** P08020-P08020.
- BREHMER, J., LOUPPE, G., PAVEZ, J. and CRANMER, K. (2020). Mining Gold from Implicit Models to Improve Likelihood-Free Inference. *Proceedings of the National Academy of Sciences* **117** 5242–5249.
- BRENIER, Y. (1991). Polar Factorization and Monotone Rearrangement of Vector-Valued Functions. *Communications on Pure and Applied Mathematics* **44** 375–417.
- BRYANT, P. E. (2018). Search for Pair Production of Higgs Bosons in the Four Bottom Quark Final State Using Proton-Proton Collisions at $\sqrt{s} = 13$ TeV with the ATLAS Detector, PhD thesis, The University of Chicago, Chicago IL.
- CACCIARI, M., SALAM, G. P. and SOYEZ, G. (2008). The anti-kt jet clustering algorithm. *Journal of High Energy Physics* **2008** 063.
- CHENG, K. F. and CHU, C.-K. (2004). Semiparametric Density Estimation under a Two-Sample Density Ratio Model. *Bernoulli* **10** 583–604.
- CHOI, S. and OH, H. (2021). Improved extrapolation methods of data-driven background estimations in high energy physics. *Eur. Phys. J. C* **81** 643.
- CMS, G. (2008). The CMS experiment at the CERN LHC. *Journal of Instrumentation* **3** S08004–S08004.
- CMS (2012). Observation of a new boson at a mass of 125 GeV with the CMS experiment at the LHC. *Physics Letters B* **716** 30–61.
- CMS (2017). Jet energy scale and resolution in the CMS experiment in pp collisions at 8 TeV.
- CMS (2018a). Observation of Higgs boson decay to bottom quarks. *Physical review letters* **121** 121801.
- CMS (2018b). Measurements of Higgs boson properties in the diphoton decay channel in proton-proton collisions at $\sqrt{s} = 13$ TeV. *Journal of High Energy Physics* **2018** 185.
- CMS (2018c). Measurements of properties of the Higgs boson in the four-lepton final state at $\sqrt{s} = 13$ TeV. *CMS PAS HIG-18-001*.
- CMS (2018d). Observation of the Higgs boson decay to a pair of τ leptons with the CMS detector. *Physics Letters B* **779** 283–316.
- CMS (2019). Measurements of properties of the Higgs boson decaying to a W boson pair in pp collisions at $\sqrt{s} = 13$ TeV. *Physics letters B* **791** 96–129.
- CMS (2022). Search for Higgs boson pair production in the four b quark final state in proton-proton collisions at $\sqrt{s} = 13$ TeV.
- COURTY, N., FLAMARY, R., TUIA, D. and RAKOTOMAMONJY, A. (2016). Optimal transport for domain adaptation. *IEEE transactions on pattern analysis and machine intelligence* **39** 1853–1865.
- CRANMER, K., PAVEZ, J. and LOUPPE, G. (2015). Approximating Likelihood Ratios with Calibrated Discriminative Classifiers. *arXiv preprint arXiv:1506.02169*.
- DE LARA, L., GONZÁLEZ-SANZ, A. and LOUBES, J.-M. (2021). A Consistent Extension of Discrete Optimal Transport Maps for Machine Learning Applications. *arXiv preprint arXiv:2102.08644*.

- DEB, N., GHOSAL, P. and SEN, B. (2021). Rates of Estimation of Optimal Transport Maps Using Plug-in Estimators via Barycentric Projections. *Advances in Neural Information Processing Systems* 34.
- DEMBINSKI, H., KENZIE, M., LANGENBRUCH, C. and SCHMELLING, M. (2022). Custom Orthogonal Weight Functions (COWs) for Event Classification. *Nuclear Instruments and Methods in Physics Research Section A: Accelerators, Spectrometers, Detectors and Associated Equipment* 167270.
- ENGLERT, F. and BROUT, R. (1964). Broken symmetry and the mass of gauge vector mesons. *Physical Review Letters* **13** 321.
- FIGALLI, A. (2010). The Optimal Partial Transport Problem. *Archive for rational mechanics and analysis* **195** 533–560.
- FLAMARY, R., COURTY, N., GRAMFORT, A., ALAYA, M. Z., BOISBUNON, A., CHAMBON, S., CHAPEL, L., CORENFLOS, A., FATRAS, K., FOURNIER, N. et al. (2021). POT: Python Optimal Transport. *J. Mach. Learn. Res.* **22** 1–8.
- FORROW, A., HÜTTER, J.-C., NITZAN, M., RIGOLLET, P., SCHIEBINGER, G. and WEED, J. (2018). Statistical Optimal Transport via Factored Couplings. *The 22nd International Conference on Artificial Intelligence and Statistics* 2454–2465.
- GHOSAL, P. and SEN, B. (2022). Multivariate Ranks and Quantiles Using Optimal Transport: Consistency, Rates, and Nonparametric Testing. *The Annals of Statistics* **50** 1012–4037.
- GOLDFELD, Z., KATO, K., RIOUX, G. and SADHU, R. (2022). Limit Theorems for Entropic Optimal Transport Maps and the Sinkhorn Divergence. *arXiv preprint arXiv:2207.08683*.
- GONZÁLEZ-SANZ, A., LOUBES, J.-M. and NILES-WEED, J. (2022). Weak Limits of Entropy Regularized Optimal Transport; Potentials, Plans and Divergences. *arXiv preprint arXiv:2207.07427*.
- GUNSILIUS, F. F. (2022). On the convergence rate of potentials of Brenier maps. *Econometric Theory* **38** 381–417.
- GUNSILIUS, F. and XU, Y. (2021). Matching for Causal Effects via Multimarginal Optimal Transport. *arXiv preprint arXiv:2112.04398*.
- HAGEDORN, R. (1964). *Relativistic Kinematics: A Guide to the Kinematic Problems of High-Energy Physics*. W.A. Benjamin.
- HANLEY, J. A. and MCNEIL, B. J. (1982). The Meaning and Use of the Area under a Receiver Operating Characteristic (ROC) Curve. *Radiology* **143** 29–36.
- HE, K., ZHANG, X., REN, S. and SUN, J. (2016). Deep Residual Learning for Image Recognition. In *Proceedings of the IEEE Conference on Computer Vision and Pattern Recognition* 770–778.
- HEINRICH, J. and LYONS, L. (2007). Systematic Errors. *Annu. Rev. Nucl. Part. Sci.* **57** 145–169.
- HIGGS, P. W. (1964). Broken symmetries and the masses of gauge bosons. *Physical Review Letters* **13** 508.
- HO, N., NGUYEN, X., YUROCHKIN, M., BUI, H. H., HUYNH, V. and PHUNG, D. (2017). Multilevel clustering via Wasserstein means. In *International Conference on Machine Learning* 1501–1509. PMLR.
- HO, N., HUYNH, V., PHUNG, D. and JORDAN, M. (2019). Probabilistic multilevel clustering via composite transportation distance. In *The 22nd International Conference on Artificial Intelligence and Statistics* 3149–3157. PMLR.
- HÜTTER, J.-C. and RIGOLLET, P. (2021). Minimax Rates of Estimation for Smooth Optimal Transport Maps. *The Annals of Statistics* **49** 1166–1194.
- HUYNH, V., HO, N., DAM, N., NGUYEN, X., YUROCHKIN, M., BUI, H. and PHUNG, D. Q. (2021). On efficient multilevel Clustering via Wasserstein distances. *J. Mach. Learn. Res.* **22** 145–1.
- KANTOROVICH, L. V. (1942). On the translocation of masses. In *Dokl. Akad. Nauk. USSR (NS)* **37** 199–201.
- KANTOROVICH, L. V. (1948). On a problem of Monge. In *CR (Doklady) Acad. Sci. URSS (NS)* **3** 225–226.
- KASIECZKA, G., NACHMAN, B., SCHWARTZ, M. D. and SHIH, D. (2021). Automating the ABCD method with machine learning. *Phys. Rev. D* **103** 035021.
- KINGMA, D. P. and BA, J. (2015). Adam: A Method for Stochastic Optimization. In *International Conference on Learning Representations*.
- KLATT, M., TAMELING, C. and MUNK, A. (2020). Empirical Regularized Optimal Transport: Statistical Theory and Applications. *SIAM Journal on Mathematics of Data Science* **2** 419–443.
- KNOTT, M. and SMITH, C. S. (1984). On the Optimal Mapping of Distributions. *Journal of Optimization Theory and Applications* **43** 39–49.
- KOLOURI, S., PARK, S. R., THORPE, M., SLEPCEV, D. and ROHDE, G. K. (2017). Optimal mass transport: Signal processing and machine-learning applications. *IEEE Signal Processing Magazine* **34** 43–59.
- KOMISKE, P. T., METODIEV, E. M. and THALER, J. (2019). Metric space of collider events. *Physical review letters* **123** 041801.
- KOMISKE, METODIEV, E. and THALER, J. (2022). EnergyFlow Python Package. <https://energyflow.network/>.
- KPOTUFE, S. (2017). Lipschitz Density-Ratios, Structured Data, and Data-Driven Tuning. In *Artificial Intelligence and Statistics* 1320–1328. PMLR.

- KUHN, H. W. (1955). The Hungarian method for the assignment problem. *Naval research logistics quarterly* **2** 83–97.
- LEE, J., DABAGIA, M., DYER, E. and ROZELL, C. (2019). Hierarchical Optimal Transport for Multimodal Distribution Alignment. In *Advances in Neural Information Processing Systems* 13453–13463.
- LIERO, M., MIELKE, A. and SAVARÉ, G. (2018). Optimal Entropy-Transport Problems and a New Hellinger–Kantorovich Distance between Positive Measures. *Inventiones mathematicae* **211** 969–1117.
- LYONS, L. (1989). *Statistics for Nuclear and Particle Physicists*. Cambridge University Press.
- MAKKUVA, A. V., TAGHVAEI, A., OH, S. and LEE, J. D. (2019). Optimal transport mapping via input convex neural networks. *arXiv:1908.10962 [cs, stat]*. arXiv: 1908.10962.
- MANOLE, T., BALAKRISHNAN, S., NILES-WEED, J. and WASSERMAN, L. (2021). Plugin Estimation of Smooth Optimal Transport Maps. *arXiv preprint arXiv:2107.12364*.
- MARTIN, B. R. and SHAW, G. (2017). *Particle Physics*. John Wiley & Sons.
- DI MICCO, B., GOUZEVITCH, M., MAZZITELLI, J. and VERNIERI, C. (2020). Higgs boson potential at colliders: Status and perspectives. *Reviews in Physics* **5** 100045.
- MONGE, G. (1781). Mémoire sur la théorie des déblais et des remblais. *Histoire de l'Académie Royale des Sciences de Paris*.
- NATH, J. S. and JAWANPURIA, P. (2020). Statistical Optimal Transport posed as Learning Kernel Embedding. *arXiv:2002.03179 [cs, stat]*. arXiv: 2002.03179.
- PANARETOS, V. M. and ZEMEL, Y. (2019a). Statistical Aspects of Wasserstein Distances. *Annual Review of Statistics and Its Application* **6** 405–431.
- PANARETOS, V. M. and ZEMEL, Y. (2019b). *An Invitation to Statistics in Wasserstein Space*. Springer.
- PELE, O. and WERMAN, M. (2008). A Linear Time Histogram Metric for Improved Sift Matching. In *European Conference on Computer Vision* 495–508. Springer.
- PELEG, S., WERMAN, M. and ROM, H. (1989). A Unified Approach to the Change of Resolution: Space and Gray-Level. *IEEE Transactions on Pattern Analysis and Machine Intelligence* **11** 739–742.
- PERROT, M., COURTY, N., FLAMARY, R. and HABRARD, A. (2016). Mapping Estimation for Discrete Optimal Transport. In *Advances in Neural Information Processing Systems* 29 (D. D. Lee, M. Sugiyama, U. V. Luxburg, I. Guyon and R. Garnett, eds.) 4197–4205. Curran Associates, Inc.
- PEYRÉ, G. and CUTURI, M. (2019). Computational optimal transport. *Foundations and Trends® in Machine Learning* **11** 355–607.
- PIVK, M. and LE DIBERDER, F. (2005). sPlot: A Statistical Tool to Unfold Data Distributions. *Nuclear Instruments and Methods in Physics Research Section A: Accelerators, Spectrometers, Detectors and Associated Equipment* **555** 356–369.
- PLACAKYTE, R. (2011). Parton Distribution Functions. *arXiv preprint arXiv:1111.5452*. arXiv: 1111.5452.
- QIN, J. (1998). Inferences for Case-Control and Semiparametric Two-Sample Density Ratio Models. *Biometrika* **85** 619–630.
- RAKOTOMAMONJY, A., FLAMARY, R., GASSO, G., ALAYA, M. Z., BERAR, M. and COURTY, N. (2022). Optimal Transport for Conditional Domain Matching and Label Shift. *Machine Learning* **111** 1651–1670.
- RAMDAS, A., TRILLOS, N. and CUTURI, M. (2017). On Wasserstein Two-Sample Testing and Related Families of Nonparametric Tests. *Entropy* **19** 47.
- REDKO, I., HABRARD, A. and SEBBAN, M. (2017). Theoretical analysis of domain adaptation with optimal transport. In *Joint European Conference on Machine Learning and Knowledge Discovery in Databases* 737–753. Springer.
- REISS, R. D. (2012). *A course on point processes*. Springer Science & Business Media.
- RIPPL, T., MUNK, A. and STURM, A. (2016). Limit Laws of the Empirical Wasserstein Distance: Gaussian Distributions. *Journal of Multivariate Analysis* **151** 90–109.
- RUBNER, Y., TOMASI, C. and GUIBAS, L. J. (2000). The Earth Mover’s Distance as a Metric for Image Retrieval. *International Journal of Computer Vision* **40** 99–121.
- SAKUMA, T. and MCCAULEY, T. (2014). Detector and Event Visualization with SketchUp at the CMS Experiment. In *Journal of Physics: Conference Series* **513** 022032. IOP Publishing.
- SCHIEBINGER, G., SHU, J., TABAKA, M., CLEARY, B., SUBRAMANIAN, V., SOLOMON, A., GOULD, J., LIU, S., LIN, S., BERUBE, P., LEE, L., CHEN, J., BRUMBAUGH, J., RIGOLLET, P., HOCHEDLINGER, K., JAENISCH, R., REGEV, A. and LANDER, E. S. (2019). Optimal-Transport Analysis of Single-Cell Gene Expression Identifies Developmental Trajectories in Reprogramming. *Cell* **176** 928–943.e22.
- VILLANI, C. (2003). *Topics in Optimal Transportation*. American Mathematical Soc. Google-Books-ID: idyFAwAAQBAJ.
- VILLANI, C. (2008). *Optimal Transport: Old and New*. Springer Science & Business Media Google-Books-ID: hV8o5R7_5tkC.
- WEISS, K., KHOSHGOFTAAR, T. M. and WANG, D. (2016). A Survey of Transfer Learning. *Journal of Big data* **3** 1–40.

YOSINSKI, J., CLUNE, J., BENGIO, Y. and LIPSON, H. (2014). How Transferable Are Features in Deep Neural Networks? In *Advances in Neural Information Processing Systems* **27**. Curran Associates, Inc.